Leveraging Surface Topologies and Additive Manufacturing for CubeSat Thermal Control

by

Michael J. Juhasz

Submitted in Partial Fulfillment of the Requirements

for the Degree of

Master of Science

in the

Mechanical Engineering

Program

YOUNGSTOWN STATE UNIVERSITY

August, 2015

Leveraging Surface Topologies and Additive Manufacturing for CubeSat Thermal Control

Michael J. Juhasz

I hereby release this thesis to the public. I understand that this thesis will be made available from the OhioLINK ETD Center and the Maag Library Circulation Desk for public access. I also authorize the University or other individuals to make copies of this thesis as needed for scholarly research.

Signature:

_____
Michael J. Juhasz, Student   Date

Approvals:

_____
Dr. Brett Conner, Thesis Advisor   Date

_____
Dr. Jae Joong Ryu, Committee Member   Date

_____
Dr. Kyosung Choo, Committee Member   Date

_____
Dr. Salvatore A. Sanders, Dean of Graduate Studies   Date

Abstract

Miniature satellites, and in particular CubeSats, have provided an economical platform to conduct experiments in a space environment for universities and small research organizations alike. This has now caught the eye of larger aerospace companies and government to develop Cubesats for a multitude of other uses. The rapid development of this platform has seen the desire to place more and more complicated experiments within the craft placing critical stress on thermal management. The small size of a CubeSat introduces size constraints of the thermal management which is also competing for real estate with other space craft sub-systems. Additive manufacturing may produce an avenue to maximize design space by incorporating complexity, in essence, for free through the process itself. This investigation looks at surface topology as a passive means to effectively dissipate waste heat for a given special constraint. The theoretical curve, given by Stefan and Boltzmann, suggests that changes to surface topology could increase heat transfer without bound. It is also investigated whether or not this can truly happen in nature. Results of numerical studies show reduction of surface temperatures by approximately 70% when compared to typical planar geometry used presently on CubeSats and full-scale satellites.

Acknowledgements

Table of Contents

List of Figures

List of Tables

Chapter 1: Introduction

The management and control of thermal energy of a satellite is a major factor in overall mission success. Prudent satellite thermal design guarantees reliability of the payload and ancillary electronics despite the variations in its environment that it will encounter. A thermal control system/subsystem (TCS) is a critical element and consideration of any spacecraft design. The primary purpose of the TCS is to maintain the temperatures of all spacecraft components within allowable operational ranges during all mission phases.

All the components of a satellite payload and ancillaries have temperature limitations. Therefore a good TCS design will effectively balance the temperature limitations of all components involved in order for the satellite to reliably operate. The table below lists the temperature limits for common satellite componentry in two different modes:

- Operating temperature: the maximum and minimum temperature limits between which components successfully and reliably meet their specified operating requirements.
- Survival temperature: the maximum and minimum temperature limits within which components are able to survive while in a power off mode, and subsequently perform as required in the operating mode.

Device	Operating Temperature (Celsius)	Survival Temperature (Celsius)
General Electronics	-40 to 85	-40 to 125
Infrared Detectors	-269 to -173	-260 to 35
Solid-state Particle Detectors	-35 to 0	-35 to 35
Batteries	-30 to 60	-50 to 60
Solar Panels	-100 to 125	-100 to 125

Like all satellite subsystems, designs that minimize cost and weight while maximizing reliability and performance are highly desirable. The design of the TCS in this regard in no different. There are two subsets of satellite thermal control strategies: Passive control and Active Control. Passive thermal control use physical principles and properties of materials without external feedback to control temperatures and operating conditions of a satellite in a continuous manner. Typical passive control elements are radiators, coatings and/or paints, phase change materials, heat pipes, and multilayer insulation (MLI). Active control is the complimentary side to passive control and uses external feedback and additional actuation to control temperatures of a satellite. Typical active control elements are louvers, resistive heaters, pumped loop cooling systems, and Peltier effect devices. In general, active thermal control produces a more stable internal satellite environment and by nature can take advantage of better performing heat transfer methods. This, though, comes with the penalty of additional complexity, cost, and weight of the system. This project entails the research and development of an additively-manufactured passive TCS design for a small satellite, namely CubeSat (Figure 1), application.
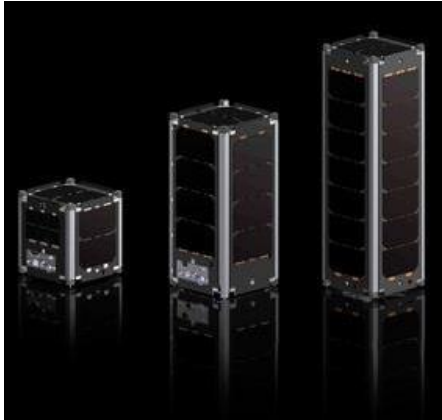
A CubeSat is a specific type of miniaturized satellite for space research that has a total volume of exactly one liter (10 cm cube), and generally has a mass of no more than 1.33 kilograms. The standard 10×10×10 cm basic CubeSat is often called a "one unit" or 1U CubeSat. They are scalable along only one axis, by 1U increments. In this way 2U CubeSat would have dimensions 20×10×10 cm and similarly a 3U CubeSat is 30×10×10 cm.

Youngstown State University (YSU) is working in partnership with the University of Texas at El Paso (UTEP), and others, on the America Makes award entitled "Printing Multi-functionality: Additive Manufacturing for Aerospace Applications." The W.M. Keck Center for 3D Innovation at is leading the development of a new multi-material, multi-technology additive manufacturing system, called Multi^{3D}. UTEP is tasked with developing an additive manufacturing cell with the capability of 3D printing multiple materials, micro-machining, and ultrasonic wire embedding to increase functionality of additive manufactured parts and assemblies. YSU is then sub-tasked with leveraging this added functionality towards development of the TCS.

For this project a passive TCS system was chosen as it seemed as the logical start off point when overlaid with the capabilities of the Multi^{3D} system. The passive TCS, in general, has other benefits than being matched to the capabilities of the Multi^{3D} system, it's lighter, more robust and reliable, and less costly as compared to active methods of thermal management. That said, the passive TCS design is not less complex. This project and research aims to take full advantage of the complexity offered by additive manufacturing by leveraging surfaces topologies for efficient thermal control.

In the following chapters a theoretical basis for CubeSat thermal control is discussed in detail. A physical model is derived using classical heat transfer theory, in which the boundary of one surface is left arbitrary to allow for investigation into surface topology. Also discussed later, the choice of surface representation and the ramifications associated. This physical model is bounded using worst-case values which are then compared to the literature. Additionally, numerical simulations were performed in Siemens NX software. Available as part of the Siemens NX software is the Space Systems Thermal Analysis module which is tailored with specific tools and options for spacecraft thermal analysis. Furthermore, an experimental study was also performed using additive manufactured test panels with different surface topologies. These panels were produced on a Stratasys Fortus 250MC, which is a fused deposition modeling (FDM) machine, using polymer as the build material. The panels then underwent testing in a retrofitted vacuum chamber of the author's design. Finally, the results from all sources were cross compared and from these data a solution for a thermal control system was decided upon.

Chapter 2: Background

2.1 Satellite Thermal Control

Satellite thermal control, like most engineering problems, is about compromise. Space, weight, and complexity of the thermal management system are weighted against the many sources of heat from individual components within the craft and from the environment as well. Much time and effort has been put into complicated thermal analysis of spacecraft, see (2), (3), (4), and (5). Engineers, generally being pragmatists, typically lump together the individual sources of heat in order to first understand the macroscopic constraints of the craft. It is from this macroscopic picture that engineers then have a toolbox of solutions which to apply to the task of thermal management. These solutions can be broken down into two general categories: Active and Passive thermal management.

2.1.1 Active Thermal Management

Active thermal management involves elements which require some form of secondary control as a response to a condition. Examples of active elements are resistive heaters, louvers, pumped loop cooling systems, and Peltier effect devices. Resistive heaters are the most common active element used on spacecraft. They come in different configurations, but all require electricity applied to resistive wires in order to generate heat and some form of control, typically a thermostat. For most space missions it is common practice to oversize the cooling elements, to account for transient effects a material degradation over time, and use heaters account for the overcooling and manage the required minimum temperature of the payload (6).

Louvers are mechanical means in which to shade and expose a surface for radiation heat transfer at favorable times. The most commonly used is the "venetian-blind" style of louver (1). Pumped loop cooling systems move a cooling fluid, usually ammonia, in order to dissipate heat generated from a spacecraft. Torres, Mishkinis, and Kaya developed a transient thermal model for such systems with validation of the model from flight data (7). Peltier effect devices use the junction of dissimilar metals, i.e. thermocouples, the either generate or dissipate heat at the component level.

2.1.2 Passive Thermal Management

Passive thermal management is accomplished with continuously operating elements and no form of secondary control. Classic passive control elements are radiators, coatings and/or paints, and phase change materials.

Most of a spacecraft's waste heat is commonly dissipated to space by radiators, which are typically of the flat plates. Since not only does a radiator need to reject internal spacecraft heat but also resist environmental heat load, the surface is frequently treated with a coating. The external surface of a spacecraft, whether radiator or not, regularly has some sort of coating and/or paint to control its thermal properties. These coatings span from exotic quartz mirrors and vapor deposited aluminum to more common white and black paints (1). Managing the combinations of coatings to ensure proper thermal is daunting and no truly unique solution exists, so it is up to the engineer to develop the solution. Phase change materials (PCMs), such as paraffin wax, represent an interesting approach to passive thermal control on a spacecraft. It allows for the storage of waste heat in the materials latent heat of melting, effectively creating a thermal capacitor. Kim, while not explicitly using

PCMs, does use the concept of a thermal capacitor to dampen transient heat loads, which he calls: Thermal Buffer Mass (8). Also, Roy and Avanic use PCMs and the concept of a thermal capacitor as a means to optimize a radiator (9).

2.2 Heat Transfer

The physical driver of any form of heat transfer is the temperature difference, and the greater the temperature difference, the larger the overall rate of heat transfer. This has analogs in electric current flow and flow through piping networks, where voltage differences drive current flow and pressure differences are the prime mover in pipe networks. In heat transfer there are three main methods of transport: conduction, convection and radiation.

2.2.1 Conduction

Conduction is the transport of thermal energy from higher energy state particles to particles of a lower energy state within a substance. Conduction can take place in all four states of matter, but in this context will be limited to solids. In solids, conduction is attributed to lattice vibrations and free electrons. Experiments have shown that for an object of a fixed length when the temperature difference is doubled, then the total rate of heat transfer is doubled. Similarly, when the object's length is doubled, the total rate of heat transfer is halved. J. Fourier first made note of these observations in 1822, and summarized them in equation form as,

$$\dot{Q}_{cond} = -kA_c \frac{dT}{dl} \ (W) \ or \ \frac{\dot{Q}_{cond}}{A_c} = \dot{q}_{cond} = -k\frac{dT}{dl} \ \left(W/m^2\right),$$

which is now known as Fourier's law of heat conduction (10). Many researchers have studied conduction and in particular optimum shapes for heat conduction. Le-

ontiou *et al.* transformed the 2-dimensional Cartesian heat conduction problem into the complex domain to find optimal shapes for heat transport (11). Their results match that of previous work and more importantly matches what would be intuitively expected. That is, for a given temperature difference, minimization of conductive path length provides the optimal solution.

2.2.2 Convection

Convection is the mode of heat transfer between a solid surface and the adjacent liquid or gas that is in motion, and it involves the combined effects of conduction and fluid motion. Depending on orbital altitude, convection can be a present factor affecting spacecraft, but for this research it is assumed to be negligible and that the craft is under vacuum conditions.

2.2.3 Radiation

Radiation is the energy emitted by matter in the form of electromagnetic waves as a response to the level of microscopic activity within a medium. Temperature is a measure of the strength of these activities, and the rate of thermal radiation emission increases with temperature (10). Since radiation is an electromagnetic effect it has a unique property that energy transport can take place between two objects through a colder medium or no medium at all, i.e. the sun heats the earth through the cold vacuum of space. Engineers are concerned with thermal transport and therefore limit themselves with electromagnetic radiation in the visible, infrared, and part of the ultraviolet light spectrum. The Stefan-Boltzmann equation for radiation heat transfer is real known to most engineers and is,

$$\dot{Q} = \sigma \varepsilon A_s (T_S^4 - T_E^4)$$

Radiation heat transfer between surfaces depends on the orientation of the surfaces relative to each other as well as their radiation properties and temperatures. This is shown in Figure 2.

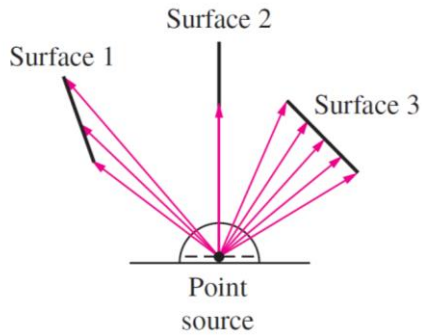Figure 2: Orientation Effect in Radiation Heat Transfer

A parameter called the view factor, Figure 3, which is only a geometric factor, accounts for the effect of orientation on radiation heat transfer between two surfaces (10) (12). This parameter has other names: shape factor, configuration factor, and angle factor. It is denoted by Fi → j, where i and j are surfaces.
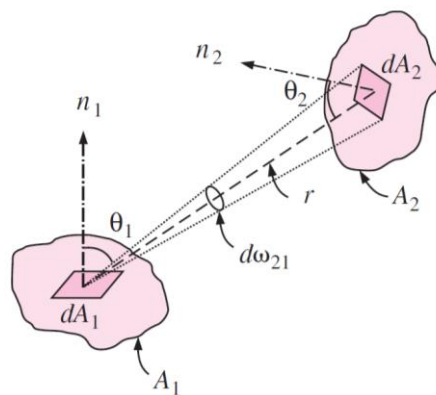

Figure 3: The View Factor

The value of the view factor ranges between zero and one. When Fi → j = 0 this indicates that the two surfaces do not have a direct view of each other, and radiation leaving surface i cannot strike surface j. On the other side, when Fi→j = 1 this indicates that surface j completely surrounds surface i, so that all of the radiation leaving surface i is received by surface j.

(a) Plane surface

$F_{1 \to 1} = 0$

(b) Convex surface

$F_{2 \to 2} = 0$

(c) Concave surface

$F_{3 \to 3} \neq 0$
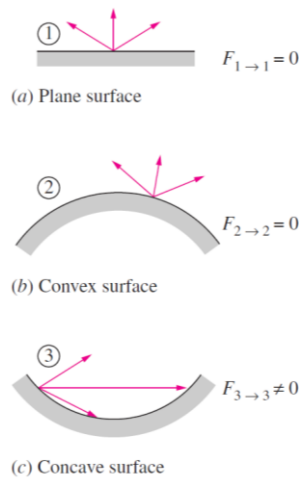
Figure 4: The View Factor in Relation to Curvature

The problem of radiation heat transfer is a difficult one. The analysis of radiation exchange between surfaces, in general, is complicated because of reflection. A beam of radiation leaving a surface may be reflected several times, with partial reflection occurring at each surface, before it is completely absorbed. This makes radiation heat transfer highly susceptible to surface condition and also to what is radiationally viewable from the surface of interest. Mathematically, thermal radiation transport constitutes as a boundary condition to differential heat diffusion equation. The difficulty in that lies with the nonlinear 4th order temperature term contained in the Stefan-Boltzmann law. In general, nonlinear equations are more difficult and te-

dious to solve, if a closed-form solution exists at all. The most commonly used meth-

od in dealing with the nonlinearity is to linearize the Stefan-Boltzmann boundary

condition and then iteratively solve for the temperature value (13) (12).

2.3 Numerical Methods

2.3.1 Finite Difference Method

The finite difference method is probably the simplest and most likely the old-

est method to discretize and solve differential equations. The technique replaces de-

rivatives of a differential equation by a divided difference quotient. In calculus, the

derivative is known by,

$$\frac{df}{dx} = \lim_{h \to 0} \frac{f(x+h) - f(x)}{h}$$

and if the limit is ignored, then this is the basis for finite difference method. The ad-

vent of finite difference techniques in numerical applications began in the early

1950s and their development was stimulated by the emergence of computers that

offered a convenient framework for dealing with complex problems of science and

technology (14). Theoretical results have been obtained during the last five decades

regarding the accuracy, stability and convergence of the finite difference method for

partial differential equations. The finite difference method process was formalized

by using a Taylor's series expansion for the derivative and this aids formulation of

higher order finite difference derivatives. The domain of a differential equation is

partitioned into a grid by the finite difference quotients and approximations of the

solution are computed at the grid points. There are two associated errors between

numerical and exact solutions inherit in the finite difference method process: trun-

cation and discretization. Truncation error comes from the use of a finite amount of terms of the Taylor's series and discretization error arises from the choice of grid spacing. Graphically, Figure 5, it is demonstrated that the choice of grid spacing is paramount for accuracy of the approximation.
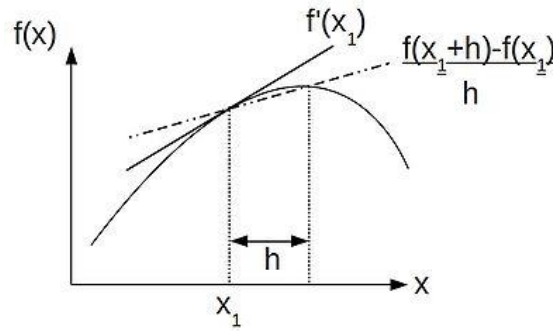

Figure 5: Finite Difference Approximation of Derivative [Source: https://source.ggy.bris.ac.uk/wiki/File:Forward-difference.jpg]

In practice, all of the methods described hereafter have a component of FDM contained within them which will allow for processing by a numerical solver.

2.3.2 Method of Weighted Residuals

The method of weighted residuals (MWR) is a class of solution techniques for partial differential equations that minimize the integral error, i.e. the residual. In general a solution to a PDE can be expressed as a superposition of a base set of functions

$$T(x,t) = \sum_{n=1}^{N} a_n(t)\varphi_n(x)$$

where the coefficients a_n are determined by a chosen method.

Let $\tilde{T}(x,t)$ be an approximation to $T(x,t)$. The residual is defined by

$R = T(x,t) - \tilde{T}(x,t)$, and if the goal is to minimize R then pre-multiplication by a weighting factor and integration over the domain of interest leads to the equation

$$\int_{\Omega} N_m \sum_{n=1}^{N} a_n \tilde{\varphi}_n \, \partial\Omega = 0.$$

The choice of weighting factors is by and large what determines the specific method of weighted residuals is being employed (14).

Such methods include:

1. the Finite Volume Method (FVM),

2. the Galerkin Method, better known as the Finite Element Method (FEM), and

3. the Boundary Element Method (BEM).

There are many other formulations of weighted residual methods, but in practice these are ones typically seen.

2.3.3 Finite Volume Method

If the weighting factor set equal to one, i.e. N_m=1. The result is the Finite Volume Method of weighted residuals. Patankar asserts that this is the preferred method in heat transfer and fluid flow problems (13). Setting the weighting factor to one has the physical meaning of preserving energy conversation in the domain of interest. Most computational fluid dynamics codes are based on FVM, however the software used in this research uses the more prevalent finite element method.

2.3.4 Finite Element Method

The Finite Element Method is the most prevalent method for solving PDEs. The formulation comes from Galerkin and it is equivalent to setting the weighting

13

factor equal to base set of functions, i.e. $N_m = a_n$ (14). This coupled with a choice of a "smart" weighting factor like orthogonal functions makes finding solutions to PDEs via computer efficient. The software used in this research relies on a FEM code to determine solutions.

2.3.5 Boundary Element Method

The Boundary Element Method (BEM) differs from the previous two methods as it not determined purely from the choice of weighting factor but is a formulation more from a perspective. The FVM and FEM are from the perspective that the equation of the domain is an approximation and the boundary conditions are exact. The BEM comes from the perspective that the equation of the domain is exact and the boundary conditions are approximate. Since the domain equation is exact, and of integral form in the context of MWR, Green's functions are required to solve integral equation. This is not always easy and straightforward, and restricts the types of problems that can be solved. There are positives to the method though; first there is reduction of spatial order by one. Secondly since the boundary conditions are to be approximated, the weighted residual techniques can be put to good use on nonlinear boundary conditions like radiation. Blobner *et al.* looked at transient heat conduction coupled with radiation problems and developed robust and stable algorithm for object of known geometry (15). One of the authors in (15), Bialecki, also wrote an informative book on the subject entitled, "Solving Heat Radiation Problems Using the Boundary Element Method (16)." Anflor and Marczak used BEM with topological sensitivity analysis in order to develop an algorithm for 2-dimensional topological optimization in heat conduction problems with conductive and convective

boundary conditions (17). They use two interesting concepts in their paper. First, is to parameterize the boundary from the discrete numerical domain to a continuous one by Bezier curves, also seen in (18). Secondly, they make use of a concept called the topological derivative in order to mechanically move the boundary and check that resulting action.

BEM is not used in this research, but could provide a fruitful avenue to explore reduction in computational cost of performing radiation calculations.

2.4 Additive Manufacturing

Additive Manufacturing (AM) is the name given to describe the technologies that build 3-dimensional objects by depositing or fusing material layer-upon-layer. AM includes many technologies such as binder jetting, directed energy deposition, material extrusion, material jetting, powder bed fusion, sheet lamination and vat photopolymerization as defined by ASTM F2792-12a (19).

The general AM part manufacturing process is as follows:

1. The part is designed in 3D CAD modeling software,

2. This CAD design is converted to Stereo Lithography (.stl) file format (more on this in Chapter 4),

3. Transfer of the .stl file to an AM machine and generation of toolpaths for the build,

4. Setup AM machine to be ready to process build,

5. Build the part,

6. Removal of the finished part,

7. Post-processing which typically includes removal of support structures.

There are small differences in this process chain that change with the type of additive manufacturing used, but for most part all techniques will adhere to this list (20).

2.4.1 Fused Deposition Modeling

Fused Deposition Modeling (FDM) is a type of additive manufacturing where a filament, most likely a polymer, is passed through an electric heater to melt the filament at which point it is then extruded through a nozzle and deposited as a layer (Figure 6). The part is then built up one layer at a time. Gibson, Rosen, and Stucker liken this to "icing a cake (20)."
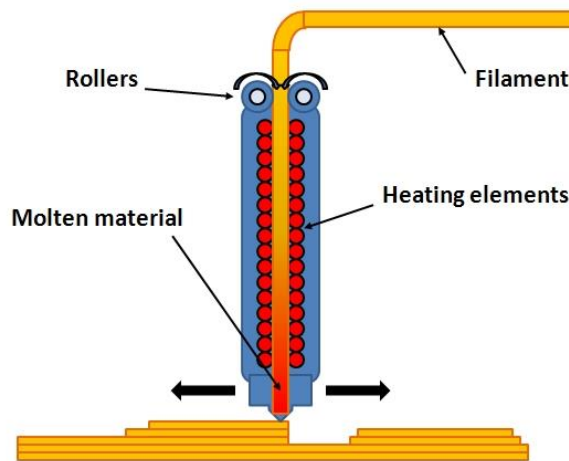
Figure 6: The FDM Process [Source: http://www.meccanismocomplesso.org/wp-content/uploads/2014/06/FDM_modeling.jpg]

The extruded molten material needs to maintain a consistent shape, while being able adhere to itself within a given layer and adhering to the previous layer. FDM requires a balance of material temperature, flow rate, and machine feed rates in order to be effective. Figure 7 shows the layer parameters of the FDM process.
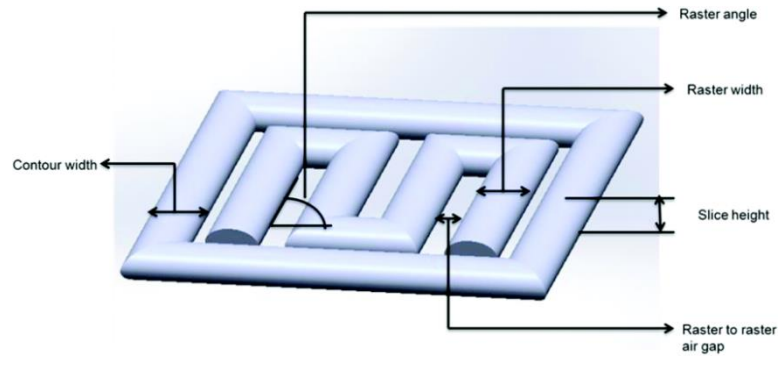
Figure 7: FDM Layer Parameters (21)

Chapter 3: Research Objectives

3.1 Rationale for this Study

Support for this research comes through an America Makes project grant entitled,"3D Printing Multi-functionality: Additive Manufacturing for Aerospace Applications." This initiative is led by University of Texas El-Paso (UTEP) and aims to expand final part functionality and multi-material usage in additive manufacturing. UTEP is working to develop a Multi3D Manufacturing System to enable the use of two FDM machines in a single build sequence and to integrate complementary technologies such as milling, and ultrasonic wire embedding. The end deliverable is the fabrication of innovative aerospace demonstrations with an application to small satellites. These include integration of electrical conduits into the vehicle structure, integration of RF antennas into the vehicle structure, and integration of thermal management into the structure. UTEP is working with other universities, YSU included, and aerospace companies to tackle this problem. YSU is specifically tasked with the development of a thermal control system.

3.2 Hypothesis

Given the small size of a CubeSat and the limited real estate available, when viewed against competing space craft sub-systems, can an effective passive thermal radiator be designed leveraging surface topology and/or surface area to dissipate waste heat?

3.3 Analysis Goals

To answer the above question radiator panels (specimens) will be designed in a Computer Aided Drafting (CAD) environment which makes use of advantageous surface topology as described by classical heat transfer theory (10). Numerical simulations will be performed using Siemens NX Space Systems Thermal Analysis to indicate trends and further develop the design. The outcome of the numerical simulations will dictate specimens to be produced for experimental study, via FDM additive method of manufacturing, in a vacuum chamber experiment designed by the author. The experimental results will be compared to those of the numerical simulation. The end deliverable being, either a standalone radiator panel, or a methodology to produce a more surface-area efficient panel tailored to the waste heat requirements of a given CubeSat and its mission.

Chapter 4: Methodology

4.1 Theoretical Analysis
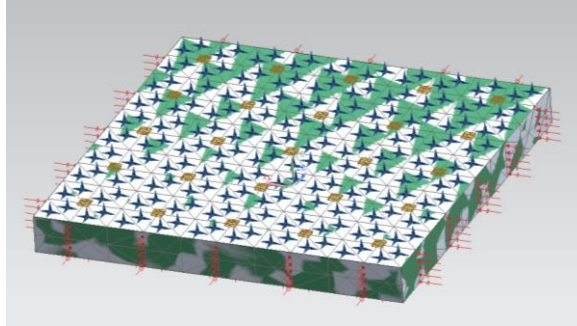
Figure 8: Base Domain of Concern

Let $T(x, y, z, t)$ be temperature as a function of spatial and time variables. Where k is thermal conductivity, ρ is the material density, and c_p is the specific heat of the material at constant pressure. The differential equation describing conduction in a medium is,

$$k_i \frac{\partial^2 T}{\partial x_i^2} = \rho c_p \frac{\partial T}{\partial t} \text{ and for steady} - \text{state}, k_i \frac{\partial^2 T}{\partial x_i^2} = 0.$$

For this problem, the sides of the specimen are insulated with the base of the specimen having an input flux placed on it and the top of the specimen is subject to a radiation boundary condition. It is therefore a safe assumption, even though it is a 3-dimensional problem, to reduce the problem to a 1-dimensional one. The equations get reduced to

$$\frac{\partial^2 T}{\partial x^2} = 0.$$

This equation has a solution $T(x) = C_1 x + C_2$ where C_1 and C_2 are arbitrary constants that must satisfy the boundary conditions:

$$1. -k\frac{\partial T(0)}{\partial x} = I, \; where \; I \; is \; the \; input \; heat \; flux, and$$

$$2. -k\frac{\partial T(\Gamma)}{\partial x} = \sigma \varepsilon T(\Gamma)^4, \; where \; \Gamma \; is \; the \; outer \; boundary.$$

Solving this equation and associated boundary conditions provided a check to validate the results of the numerical simulations.

4.2 Numerical Modeling and Simulation

4.2.1 Specimen Generation

The specimens that would later be used for simulation and manufacture were first designed using the 3D modeling software, SolidWorks. The design space of 10cm x 10cm x 1cm formed a basis for all subsequent models. This design space formed a bounding box to work within. Expanding upon the idea where radiation transport is directed effected by curvature, these geometries were investigated: convex, concave, and planar. Only using one single geometry type over the entire surface of the specimens was deemed restrictive, and therefore the specimens' surface area was subdivided into equally sized portions, initially 16 portions.

Figure 9: Examples of Convex, Concave, and Planar Specimens Generated in CAD

These portions then had one of the three geometries applied to its surface, at varying heights and this is detailed in Table 2 . These specimens served as a probe, once

simulated, that would direct future specimen design. The results of these first simulations will be discussed in detail later.

Specimen	Material	Thermal Conductivity (W/m-K)	Emissivity	Surface Area (cm^2)	Volume (cm^3)
Control	PC w/ Boron Nitride	8	0.89	100.00	100.00
Convex 16 (.125cm domes)	PC w/ Boron Nitride	8	0.89	100.64	93.06
Convex 16 (.25cm domes)	PC w/ Boron Nitride	8	0.89	102.72	86.11
Convex 16 (.5cm domes)	PC w/ Boron Nitride	8	0.89	110.56	72.22
Convex 16 (.75cm domes)	PC w/ Boron Nitride	8	0.89	122.24	58.33
Convex 16 (.875cm domes)	PC w/ Boron Nitride	8	0.89	129.28	51.39
Waffle 16 (.125cm deep)	PC w/ Boron Nitride	8	0.89	107.36	90.96
Waffle 16 (.25cm deep)	PC w/ Boron Nitride	8	0.89	113.40	83.92
Waffle 16 (.75cm deep)	PC w/ Boron Nitride	8	0.89	129.72	70.75
Waffle 16 (.875cm deep)	PC w/ Boron Nitride	8	0.89	131.84	69.96
Concave 16 (.125cm divots)	PC w/ Boron Nitride	8	0.89	100.64	94.44
Concave 16 (.875cm divots)	PC w/ Boron Nitride	8	0.89	129.28	61.11

Following the first round of results, there was not a discernible advantage to either of the geometries, with regards to a low conductivity material. Classical heat transfer theory describes convex geometry as the most beneficial (10), and since final material choice was still undecided, the next set of specimens were designed only with convex geometry. This second round of specimens held the convex dome geometry at fixed height of .5cm but varied the number of perturbations in a given panel, Figure 10. For continuity, it started with 16 convex domes then 32, 100, and

continued until 1600 domes were reached. Information about the specimens is contained in Table 3.
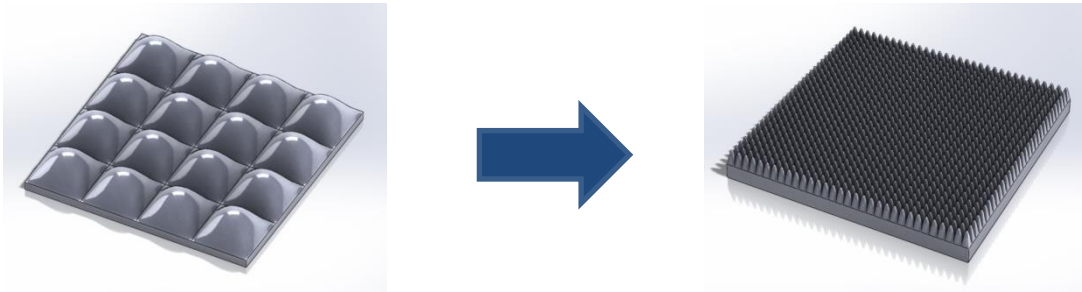
Figure 10: Convex Dimple Specimen Examples

Beyond the value of 625 convex domes, the computers in YSU's Engineering Computing Complex ran out of memory to process the models, so alternative approaches for simulation were needed.

Table 3: Convex Dimple Specimen Details

Specimen	Material	Thermal Conductivity (W/m-K)	Emissivity	Surface Area (cm^2)	Volume (cm^3)
Control	6061-T6	167	0.89	100	100.00
Convex Dimple 16	6061-T6	167	0.89	110.56	72.22
Convex Dimple 100	6061-T6	167	0.89	153.16	72.22
Convex Dimple 400	6061-T6	167	0.89	249.44	72.22
Convex Dimple 625	6061-T6	167	0.89	301.75	72.22

Since in essence there were only two criterions for the surface: 1. that it be convex in nature, and 2. that the panels exhibit ever-increasing surface area. So, a new, and final, set of specimens were designed. Ones with a fixed number of perturbations, 196, and varying the surface area was accomplished by defining the convex dome by a two-term cosine expansion.
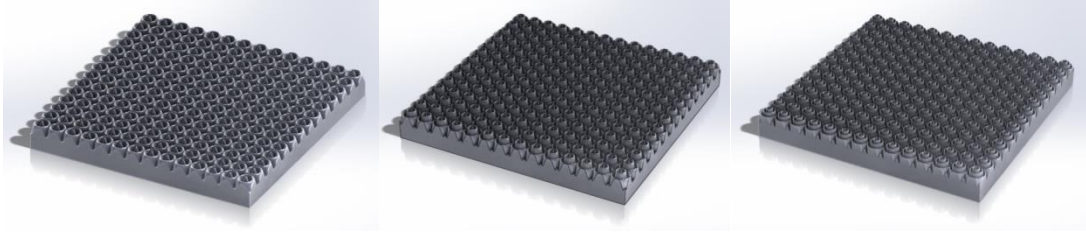
Figure 11: Examples of Convex 196 Specimens

SolidWorks allows for equation driven curves, so a curve was created across the diagonal of a base square. Table 4 gives the details of these specimens as well as the equations used to generate the geometry. These curves when revolved around the center of the base square formed the required solid geometry which was then expanded to a total of 196 copies. One-hundred and ninety-six was chosen to be a balance between having enough perturbations to achieve the required surface area and yet low enough to be computationally achievable. The surface area was then modified by manipulating the second term of the cosine expansion. All these specimens were then imported into Siemens NX 9.0 for simulation which is discussed next. The thermal conductivity for ABS is .17 W/m*K which was supplied from the Siemen's material library and closely matched research on thermal conductivity of ABS polymers used in additive manufacturing conducted by Dr. Corey Shemelya at UTEP.

Table 4: Convex 196 Specimen Details

Specimen	Material	Thermal Conductivity (W/m-K)	Emissivity	x Parameter Span	Two-Term Expansion Equation	Surface Area (cm^2)	Volume (cm^3)
Control	ABS	0.17	0.84	NA	NA	100	100
T196P197	ABS	0.17	0.84	-0.50507627 to .50507627	.35*cos(x/.42)+.15*cos((9*x)/.50507627)	197	100
T196P226	ABS	0.17	0.84	-0.50507627 to .50507627	.35*cos(x/.42)+.15*cos((10*x)/.50507627)	226	100
T196P356	ABS	0.17	0.84	-0.50507627 to .50507627	.45*cos(x/.33)+.15*cos((17.75*x)/.50507627)	356	100
T196P368	ABS	0.17	0.84	-0.50507627 to .50507627	.45*cos(x/.31)+.15*cos((18.25*x)/.50507627)	368	100
T196P507	ABS	0.17	0.84	-0.50507627 to .50507627	.45*cos(x/.32)+.15*cos((26*x)/.50507627)	507	100

4.2.2 Simulation Process

All the simulations were performed in NX Space Systems Thermal (NXSST) Analysis Module for Siemens NX 9.0. Like most simulation packages the process flow is for NXSST:

1. Import geometry,

2. Apply a finite element mesh to said geometry,

3. Apply boundary conditions,

4. Setup the solver and solve, and

5. Post-process the results.

4.2.3 Meshing

After importing a specimen, a finite element mesh was applied to the geometry in a three step process. First, a base 3D tetrahedral mesh was selected and applied. Tetrahedrals are generally not good elements from and accuracy point of view, since they vary linearly across the element. To combat this problem, a tetra-

hedral element with midside nodes was used which allows for a parabolic variance across the element increasing its accuracy. These midside nodes can be moved to better fit the geometry by distorting the tetrahedral, but it was decided not to use this ability of the node because it does introduced some error in the transformation equations which is dependent on the amount of distortion. A mesh size of 5mm was chosen in order to "rough in" the geometry. This size is obviously too large to capture most of the detail of the surface topology, but is perfectly fine for most places within the interior of the specimen. Application of a 2D surface mesh is the second step in the process. This 2D mesh provides seed nodal points where the 3-dimensional mesh can then build off of, and this is how the accuracy of the surface topology can be recovered creating a mesh of proper quality. Mesh size of the 2D surface mesh varied between 1mm and .25mm depending on what the computers could process. The last step in the meshing process is to update the 3D tetrahedral mesh with the new seed points generated by the 2D mesh. Figures 12-16 show the results of this meshing process with NXSST. The meshes in Figures 12-14 very regular and represent the surface topology well. All the meshes are free-mapped so within the solid the some variance in the element structure, but visually don't appear be highly distorted. The problems that occurred with the meshes are centered on the 2D surface mesh. In Figure 14, this starts to become apparent with what looks like little chips in the otherwise smooth surface. Then progressing through Figure 15, this chipping becomes worst until in Figure 16 the geometry of the original CAD model is completely lost. The fix for the problem is mesh refinements, but this could not be achieved due to computational limitations.
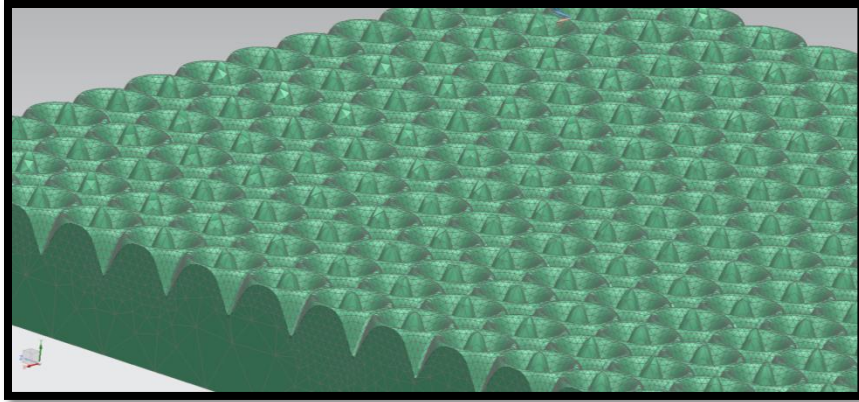
Figure 12: 3D Tetrahedral Mesh of T197P197
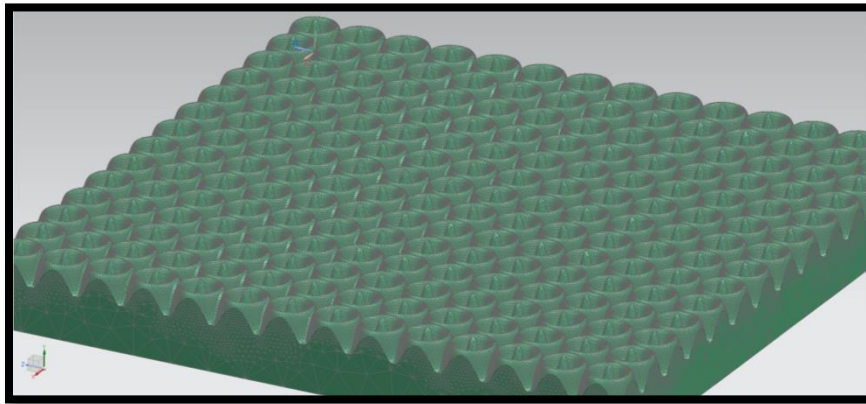
Figure 13: 3D Tetrahedral Mesh of T196P226
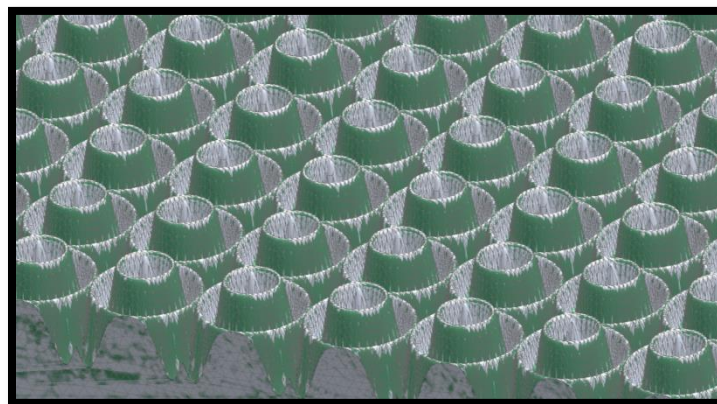
Figure 14: 3D Tetrahedral Mesh of T196P356
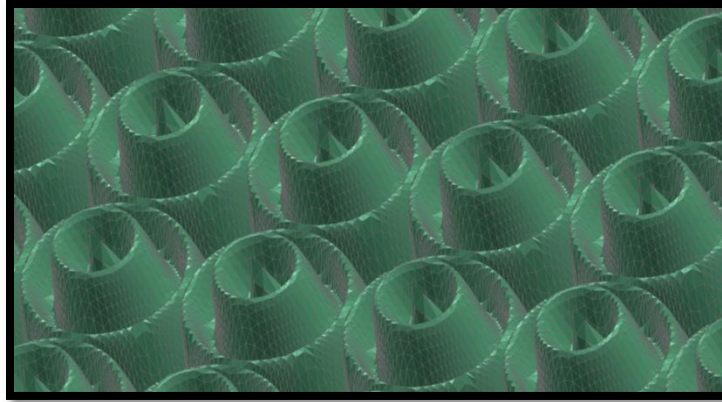
Figure 15: 3D Tetrahedral Mesh of T196P368
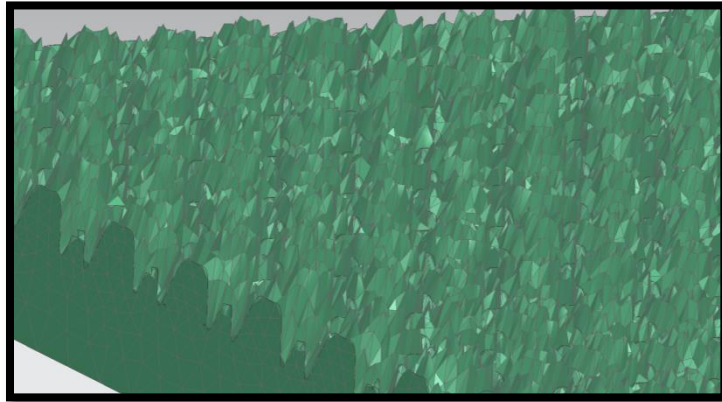
Figure 16: 3D Tetrahedral Mesh of T196P507

The table **Error! Reference source not found.** summarizes the finished meshes of the specimens of concern.

Table 5: Mesh Results

Mesh Results		
Part Identifier	# of Elements	# of Nodes
Control	3824	5607
T196P197	525,991	684,435
T196P226	1,319,895	1,705,708
T196P356	4,110,463	5,390,391
T196P368	4,275,240	5,610,092

T196P507	485,108	642,939

4.2.4 Boundary Conditions

After meshing any specimen the next step to apply boundary conditions. While not necessarily a boundary condition, first the material of the specimen was defined. For the steady-state simulation of the specimens 6 boundary conditions are required for an object that is generally cubic; a boundary condition for every face.
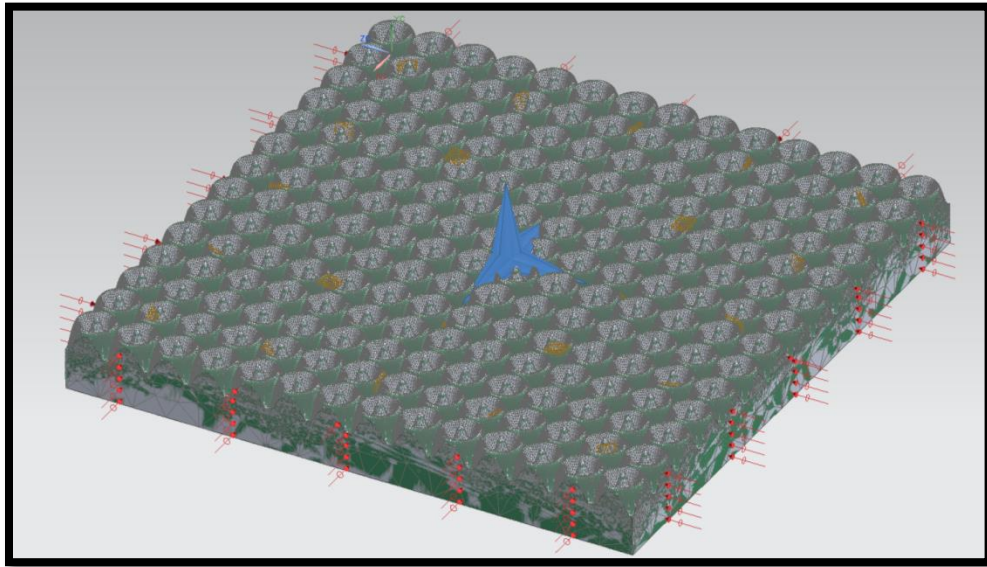
Figure 17: T196P226 with Associated Boundary Conditions

Figure 17, above, illustrates the boundary conditions placed on all the steady-state specimens. Viewable in Figure 17 are the four insulated boundary conditions on the sides, the radiation boundary condition from the convex surface. The radiation boundary was set with an effective emissivity of .84 and a moderately high level of precision, the software comes preset which 5 levels of precision and 4 was selected (22). Not shown is the 20W heat input boundary condition which is distributed

evenly along the base of the specimen. Lastly there is a seventh boundary condition, NXSST refers to it as a simulation object called, radiation element subdivision. Radiation element subdivision augments the radiation boundary condition to include mutual irradiance and shadow zones caused by non-flat geometries. Once the boundary conditions were set, the solver is next to be set up.

4.2.5 Solver Setup

The solver that NXSST provided is pre-programmed and for most intents and purposes it is not necessary to make changes to the solver. That said, after trial error, reducing the convergence criteria from a change in temperature of .001 to .1 was the only way the stay as consistent as possible with the meshes and boundary conditions, and still yield a solution without running out of computer memory. These simulations required delicate balance of multiple variables in order for the computer to process the data.

4.3 Experimentation and Specimen Manufacture

4.3.1 Additive Manufacture of Specimens

The process of creating an additively manufactured part has many parallels to traditional manufacturing and in particular CNC manufacturing. That process is as follows:

1. An electronic part is created using CAD,

2. A file conversion takes place to allow the CAD part to be recognized by CAM software,

3. CAM software processes the data and creates the required toolpaths for manufacture,

4. The toolpaths are transferred to a machine tool for manufacture and the part is created.

In our case, the specimens already produced for numerical simulation are converted into a stereo lithography file type (.stl). The stereolithographic file conversion performs a tessellation on the object of interest with the normal of each triangle oriented outward (23). This file format is readily accepted by Stratasys's Insight CAM software. The software packages Insight and Control Center by Stratasys were provided with the purchase of the Fortus 250MC FDM printer (Figure 21), and operate as a system. Once the stl-file is imported into Insight is then oriented by the user. For the thermal experiment, the specimens were oriented in two directions. Looking down from the top of the Fortus 250MC, the parts were oriented with the convex surface facing the onlooker (XY orientation) and parallel to the plane of the build plate or with a profile view of the convex surface facing the onlooker (Z orientation) and orthogonal to the plane of the build plate shown in Figure 18.
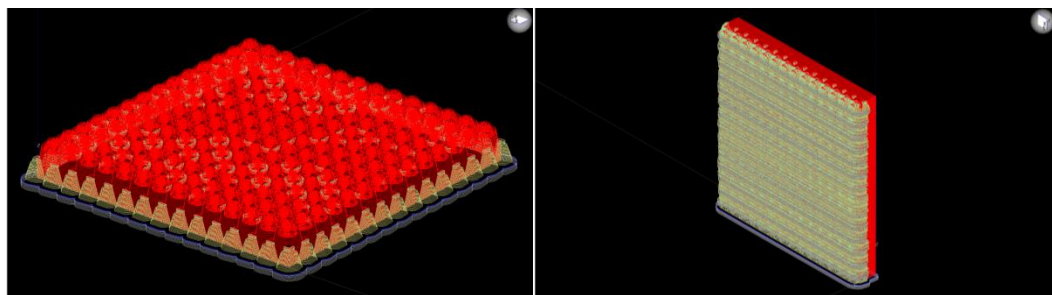
Figure 18: Examples of Print Orientation (XY on Left, Z on Right)

The oriented stl-file is then sliced in the z-axis at the machine specified slice height of .254mm. The slice height is fixed by the machine z-axis resolution. These slices

are then converted into two-dimensional contours on which the toolpaths will be created (Figure 19). Supports required to build the geometry are also created in the Insight software package.
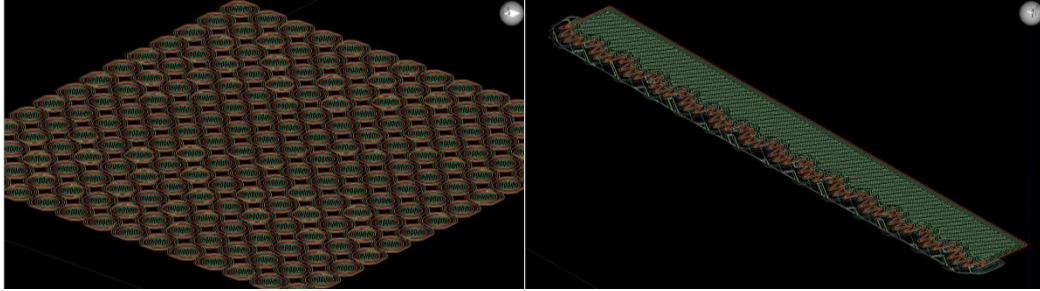
Figure 19: Examples of Toolpaths within Contours

For accuracy and density, the specimens were made using a solid fill and the smallest raster spacing. The toolpath settings are shown in Figure 20.
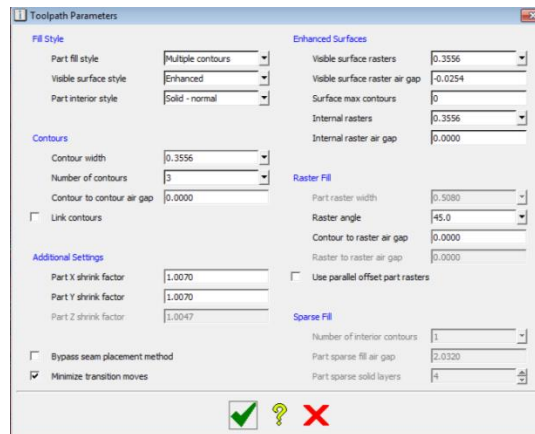
Figure 20: Toolpath Parameters

The build time on twelve specimens, six printed in XY and six printed in Z orientations, was roughly 7 days, and they were printed in ABSplus-P430 filament that was ivory in color. After completion of the build, the specimens were placed in a heated chemical bath in order to remove the added supports.

Figure 21: Stratasys Fortus 250MC

In Figure 22, some of the final manufactured specimens are shown. Due to light ivory color of the specimens, it is difficult to accurately view the final build quality from the photos, but there were differences between the XY and Z printed specimens. These differences are more easily seen in the SEM micrographs of Figure 23 and Figure 24.
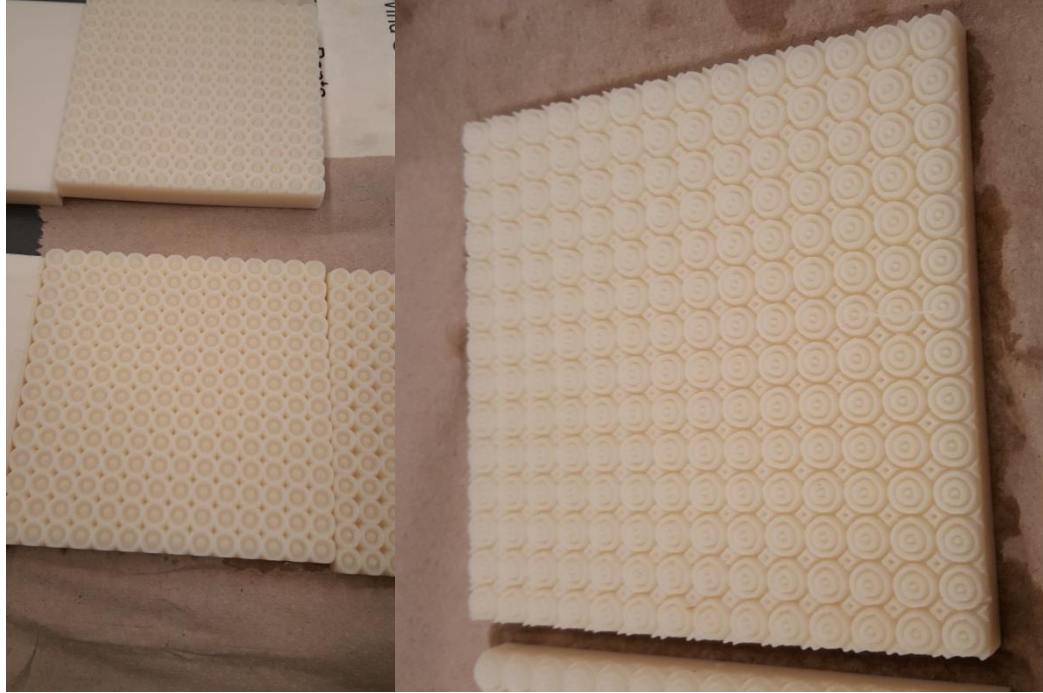
Figure 22: Specimens printed on the Fortus 250MC

Figure 23 is a comparison of the build quality of T196P356. On the left-hand side,

the surface is generally smoother than that on the right-hand side, but at the cost of

losing accuracy of the surface. It appears that even at the smallest setting the depos-

ited line width was still too large to capture the original CAD models geometry.

There is also a diagonal deformation due to the entry/exit of the print head. The Z

printed specimen more closely follows the original CAD model's geometry.
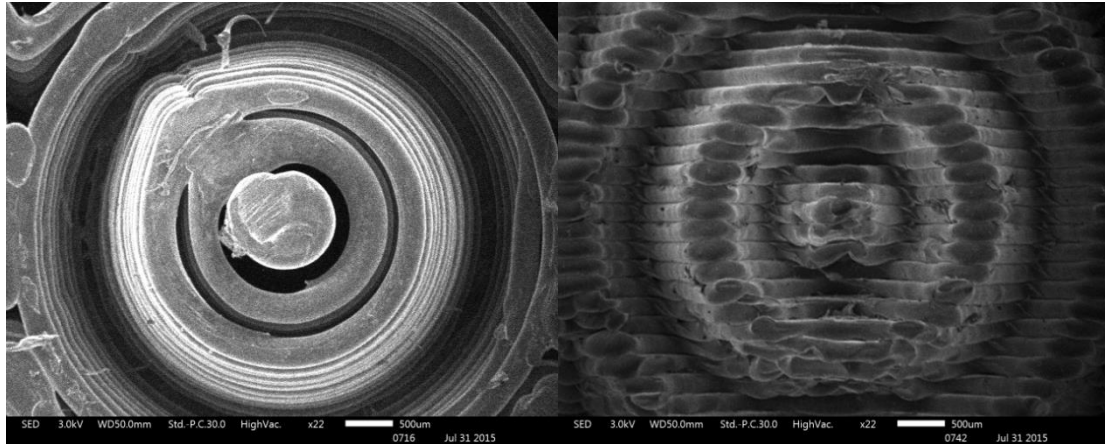
Figure 23: Comparison of T196P356 (XY) and T196P356 (Z)

Figure 24 is the same subject matter as Figure 23, but with the specimens tilted at 10 degrees to give dimensionality to the surface topology.
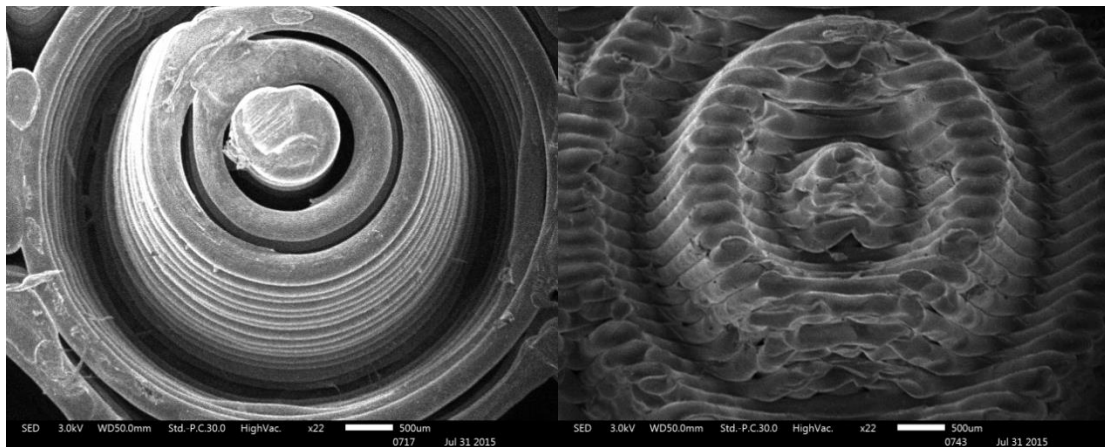
Figure 24: Comparison of T196P356 (XY) and T196P356 (Z) at 10 degrees of tilt

Figure 25 is a series of micrographs of increasing magnification. The aim was to display the interlayer bonding. In general the FDM process produces parts with directional material properties. Individual build layers are more cohesive and exhibit better properties when compared to those of layer-to-layer (20). This is not limited to only mechanical properties as thermal properties also exhibit anisotropy. The close-

up of the interlayer bonds in Figure 25 support this claim as pseudo contact con-

ductance has been introduced to the system yielding low values of conductive heat

transport in that along that direction.
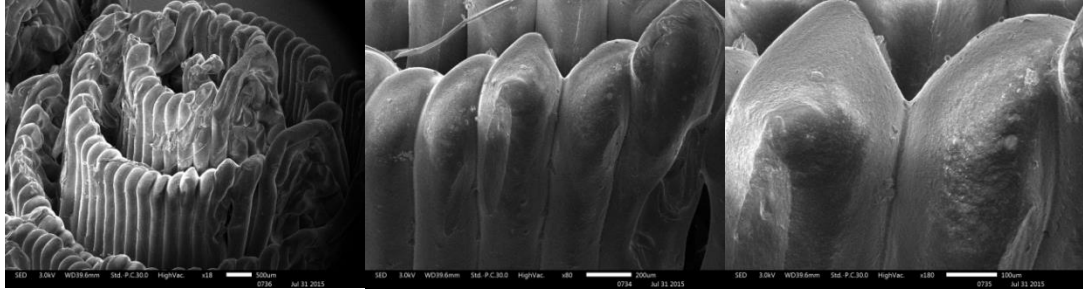
Figure 25: Layer Bonding of T196P507

Lastly, in Figure 26 at the front of each protrusion there is better homogeneity of the

material in an individual layer. These factors make the case that the more homoge-

neous connection between source heat at the base of the panel to the radiating sur-

face, i.e. Z oriented build direction, and better surface resolution will yield a higher

rate of heat transport.
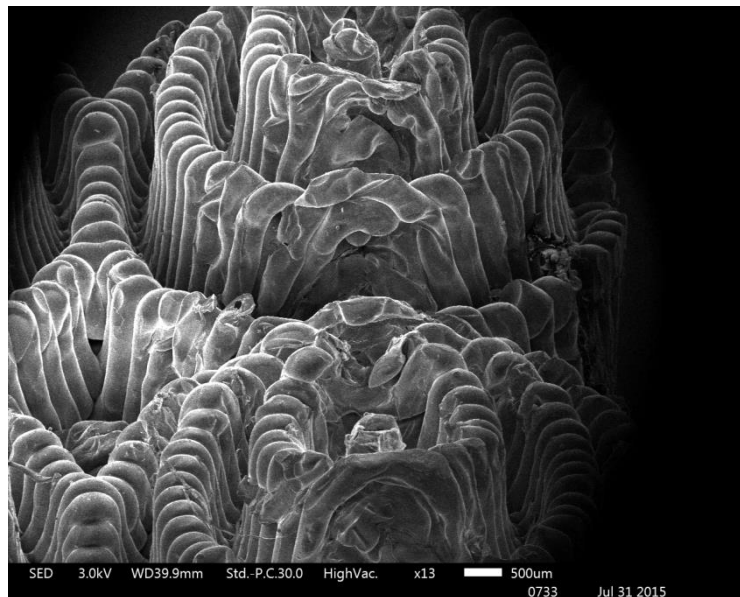
Figure 26: Micrograph of two surface protrusions on T196P507

4.3.2 Experimental Test Chamber

Conducting an experiment on the specimens required repurposing of a vacuum molding machine. Creating an experiment with space-like conditions was not feasible, but reworking a vacuum molding machine to at least eliminate convection seemed like a plausible endeavor. Figure 27 shows the proposed test chamber modifications. The specimen would be placed on a heat source, i.e. hot plate, while at the top of the chamber a liquid nitrogen cooled heatsink would provide the necessary temperature difference for radiation transport. In the center of the heatsink is an aperture where a thermopile can record the incoming irradiance. A restriction on the design of this experiment was also to retain the vacuum molder's original functionality, so no permanent modifications would be made.
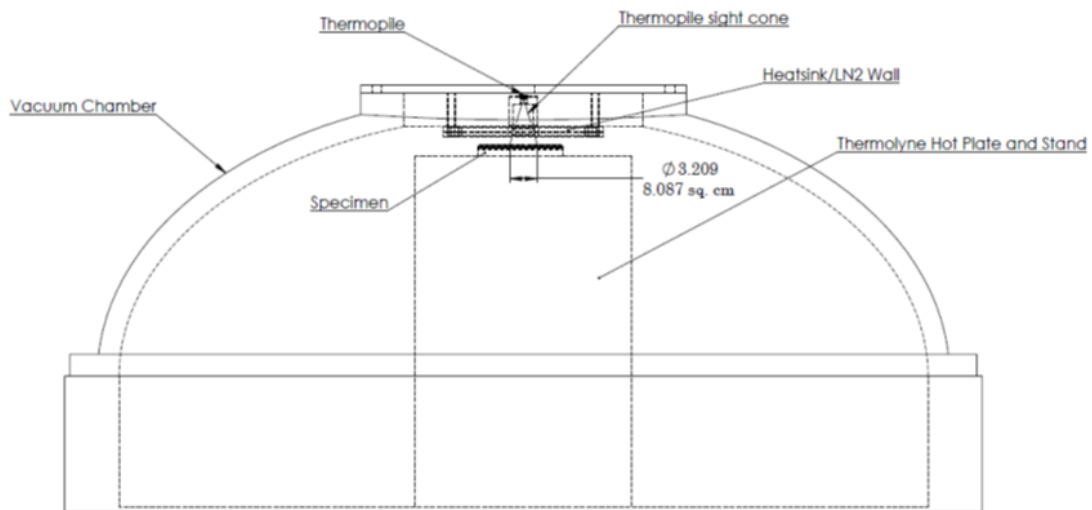
Figure 27: Layout of Experimental Test Chamber

37

Figure 28 is a blueprint of the liquid nitrogen heatsink, which was machined by

Kiraly Machine from aluminum 6061-T6. The heatsink was attached to a newly-

fabricated HDPE lid using aluminum standoffs and fasteners.
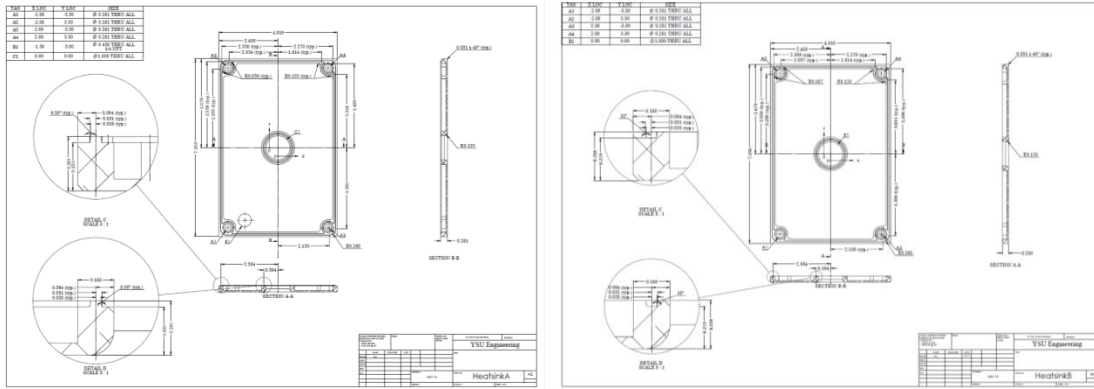
Figure 28: Blueprint of LN2 Heatsink

Closed-cell foam insulation was applied to the back of the heatsink to isolate the

thermopile from intense cold of the liquid nitrogen. The thermopile was supplied by

Dexter Research and included an amplifier. It was located centrally on the back of

the heatsink.
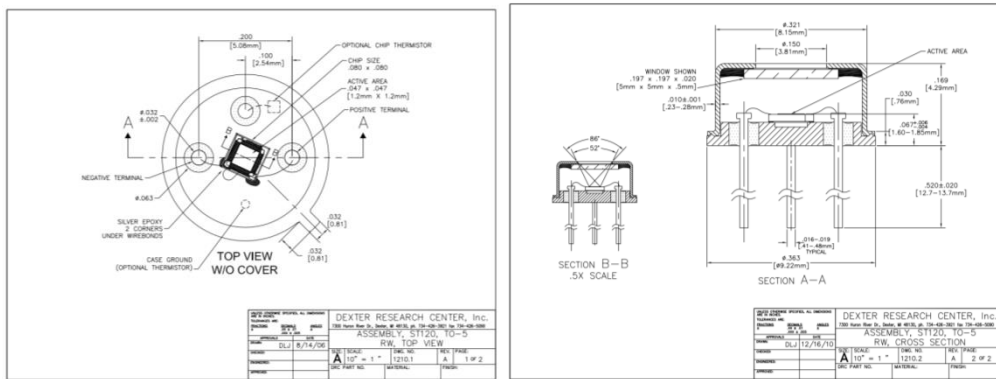
Figure 29: Blueprints of Dexter Research Thermopile

Figure 30: Experimental Test Chamber and Ancillary Equipment

Figure 30 displays the modified vacuum molder. Originally the dome on the molder

was a clear polymer, but it was coated with a black plasticized paint which was to

minimize reflections and also permit easy removal. A replacement vacuum gauge

was attached to better monitor the vacuum level within the chamber. Inside the

chamber sits a Thermolyne hot plate which was preset and never altered for all the

testing. The hot plate was preset using a Fluke infrared thermometer to 65 degrees

Celsius. An Omega thermistor was affixed, Figure 31, using thermally conductive epoxy to the hot plate.

Figure 31: Thermolyne Hot Plate with Omega Thermistor Attached

The Omega thermistor required a whetstone bridge circuit to facilitate use with the data acquisition system. 2400 ohm resistors formed three legs of the circuit with the thermistor completing it. Thermistors have a nonlinear resistance response to temperature. In Table 6 Omega provides these resistance values based on temperature and Figure 32 is a graphical representation of the information provided for the specific thermistor used in this experiment.

Figure 32: Thermistor Temperature vs. Voltage

A National Instruments NI-DAQ data acquisition system was used for data collection. It connects to a PC via a USB connector, and the signals are processed and rec-

orded with LabView 2.0 software package. The entire data acquisition setup can be seen in Figure 33.

Figure 33: View of Data Acquisition System Wired with Sensors

4.3.3 Sample Preparation

Sample preparation was simple and straightforward, and only required attaching a thermistor to the surface using thermally conductive epoxy. The thermistor was placed on a similar location for specimens tested, roughly 1.5cm x 1.5cm from the edges of the specimen. This is shown in Figure 34.
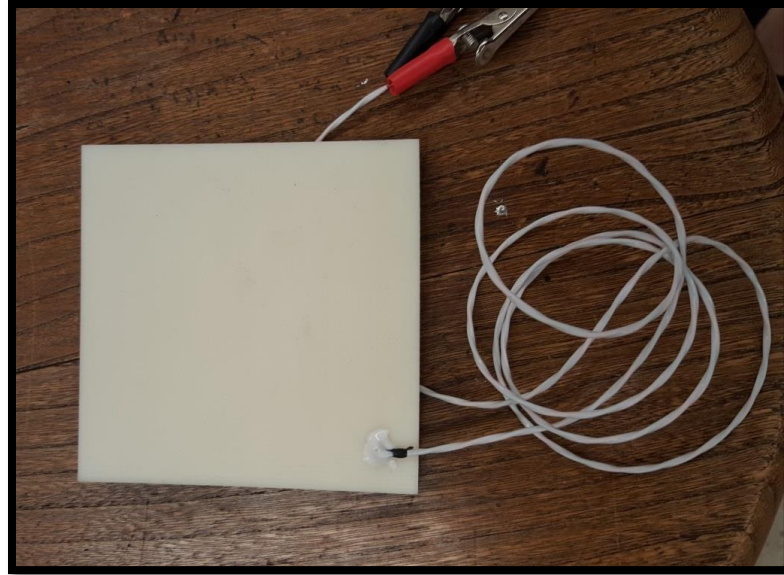
Figure 34: Attachment of Thermistor to Specimen

4.3.4 Experimental Procedure

The experimental proceeds step-by-step as follows:

1. Calibration of thermistors at room temperature to account for discrepancies in circuit connection (adjustment to resistance in the circuit).

2. Installation of the specimen inside the chamber on top the hotplate, surface-to-contact only. (Figure 35)
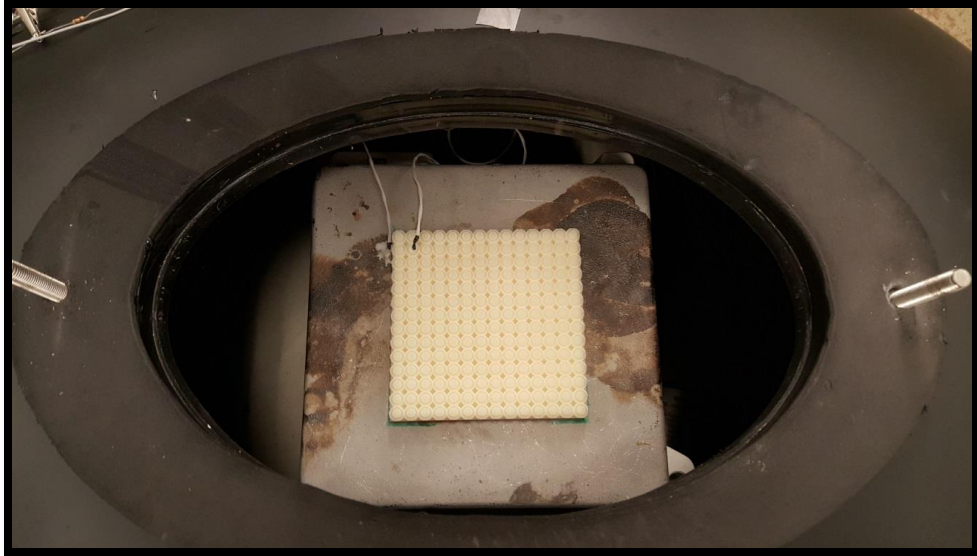
3. Attach lid containing heatsink a thermopile.

4. Fill heatsink with liquid nitrogen.

5. Turn on vacuum pump.

6. Begin recording data once vacuum pressure has reached -0.9 MPa gauge to establish baseline until -1.0 MPa gauge pressure is reached.

7. Turn on hot plate.

8. Record data until hot plate and specimen thermistors reach a relative equilibrium.

9. Turn off hot plate and bring chamber back to atmospheric pressure.

Chapter 5: Results and Discussion

5.1 Numerical Simulation Results and Discussion

For each of the three different studies, and analytical hand calculation was performed of a control specimen, 10cm x 10cm x 1cm thick, to ascertain the correctness of the software's output. Due to the insulated edge boundary condition on all of the specimens, for simplicity 1-dimensional heat transfer was assumed and the correlation between the analytical and simulation result bears out this assumption. The 1-dimensional steady state heat equation is given by,

$$\frac{\partial^2 T}{\partial x^2} = 0$$

with the general solution of

$$T(x) = C_1 x + C_2.$$

C_1 and C_2 are arbitrary constants that must satisfy the boundary conditions. Those boundary conditions being,

$$at\ x = 0:\ -k\frac{\partial T(0)}{\partial x} = I, where\ I\ is\ a\ known\ input\ flux,$$

$$and\ at\ x = L:\ -k\frac{\partial T(L)}{\partial x} = \sigma\varepsilon T(L)^4.$$

Working through one control specimen as an example,

$$let\ k = 8\left(\frac{W}{m^2 * K}\right), I = 2000\left(\frac{W}{m^2}\right), L = .01\ (m), \sigma = 5.67E^{-8}, and\ \varepsilon = .89.$$

$$Therfore, C_1 = \frac{I}{-k} = -250\ and\ (-2.5 + C_2)^4 = \frac{kC_1}{\sigma\varepsilon} \rightarrow C_2 = 448.684.$$

$$Hence\ T(x) = -250x + 448.684\ with\ T(0) = 448.684\ (K)$$

$$= 175.684\ (C)\ and\ T(.01) = 446.184\ (K) = 173.184\ (C).$$

The simulation is validated when comparing the above results with Table 7. Similarly, the other two simulation studies are validated in the same manner.

Also performed on all three studies, was a comparison between simulation surface temperature and that given the Stefan-Boltzmann equation for radiative heat transfer. The curve generated by varying the surface area in the equation acted as guide in the analysis of the results. Those two equations are shown in order now,

$$\dot{Q}_{rad} = \sigma \varepsilon A_s T_s^4 \ and$$

$$T_s(A_s) = \sqrt[4]{\frac{\dot{Q}_{rad}}{\sigma \varepsilon A_s}}.$$

5.1.1 Convex, Concave, and Planar Results and Discussion (Study 1)

The convex, concave, and planar specimens with 16 entities of varying height, Figure 36, was the first numerical simulation study performed.

Figure 36: Convex, Concave, and Planar Specimen Examples

The results of the simulations, shown both graphically and in tabular form in Figure 37 and Table 8, display decreasing average surface temperatures, as result of increasing surface area. These results closely, if not exactly, follow the theoretical Stefan-Boltzmann curve, lending credence to the results. It is of note that this decrease in surface does not seem to be related to curvature whatsoever. The thought

is that the low conductivity of this material drives the indifference to curvature. Said another way, with a poorly conducting material any increase in surface area, regardless of shape, increases radiative heat transfer. It is the realization that lead to the second numerical study where the curvature entities are held to a fixed height but the number of these entities is drastically increased and therefore in significant increase in surface area.
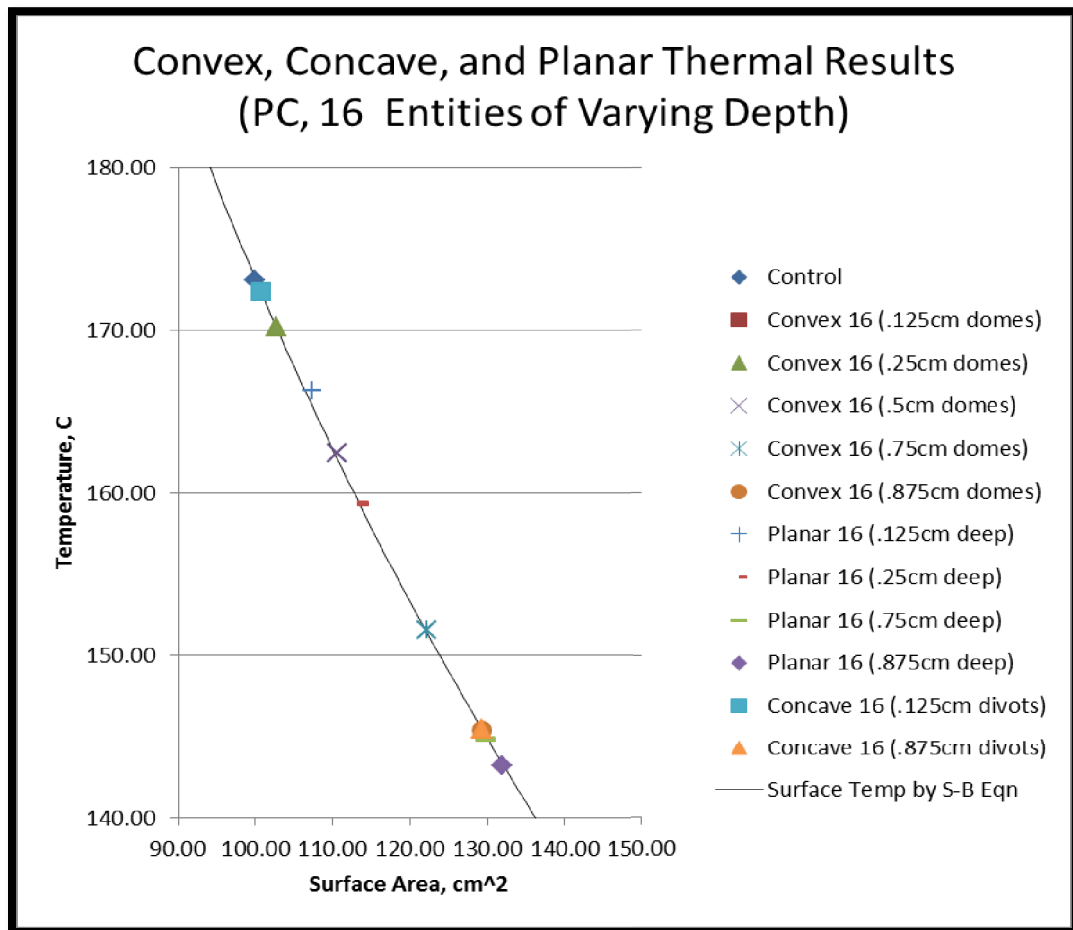
Figure 37: Convex, Concave, and Planar Results

47

Convex, Concave, and Planar Thermal Results (ABS, 16 Entities of Varying Depth)					
Specimen	Surface Area (cm^2)	Volume (cm^3)	Base Temp, Celsius	Surface Temp, Celsius	Delta Temp
Control	100.00	100.00	175.55	173.05	2.50
Convex 16 (.125cm domes)	100.64	93.06	174.66	172.37	2.29
Convex 16 (.25cm domes)	102.72	86.11	172.33	170.23	2.09
Convex 16 (.5cm domes)	110.56	72.22	164.12	162.41	1.72
Convex 16 (.75cm domes)	122.24	58.33	152.87	151.50	1.37
Convex 16 (.875cm domes)	129.28	51.39	146.60	145.38	1.22
Planar 16 (.125cm deep)	107.36	90.96	167.82	166.28	1.54
Planar 16 (.25cm deep)	113.40	83.92	161.52	159.34	2.18
Planar 16 (.75cm deep)	129.72	70.75	146.62	144.80	1.82
Planar 16 (.875cm deep)	131.84	69.96	144.92	143.18	1.74
Concave 16 (.125cm divots)	100.64	94.44	174.74	172.36	2.38
Concave 16 (.875cm divots)	129.28	61.11	147.11	145.45	1.66

5.1.2 Convex Dimple Numerical Simulation Results and Discussion (Study 2)

The second study performed was on specimens where the number of convex dimples was varied and the height of the dimple remained constant. In this study a material change took place which was the result YSU speaking with NASA Glenn Research Center on a collaborative CubeSat project where for NASA's needs material choice was not restricted. Subsequently, 6061-T6 aluminum was chosen as the material of interest as it common in satellite construction and has high thermal conductivity. Also, because of the increase in thermal conductivity the switch was made to purely convex curvature for the dimples. The previous study shows that curvature

was not a physical driver in low conductivity materials, but it was thought that significant increase in the thermal conductivity of a material would make curvature choice more of a factor. Figure 38, displays a specimen with 1024 dimples on the surface and is typical of the other specimens up the numbers of dimples on the panel.
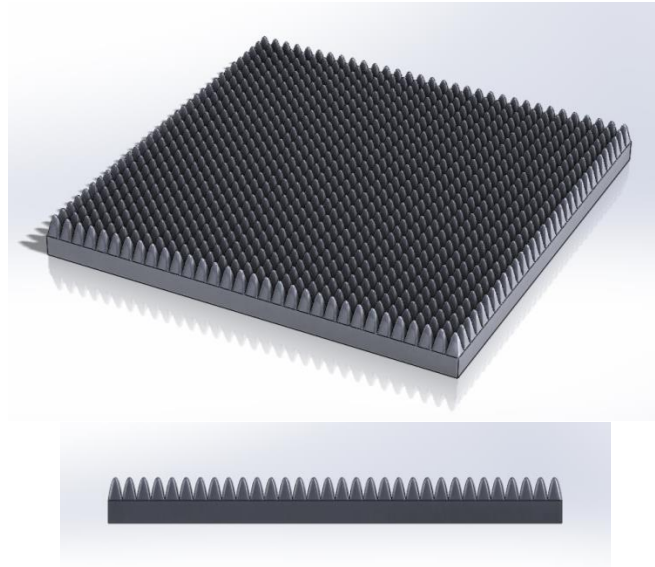
Figure 38: Convex Dimple Specimen shown both in Isometric and Profile

The results of this numerical simulation study are shown graphically in Figure 39 and in tabular form in Table 8. Again, what is given are average surface temperatures.

In general, the results conform to the theoretical curve given by the Stefan-Boltzmann equation. It is the last two data points, specimens Convex Dimple 400 and Convex Dimple 625, which are of interest because they start to deviate from the theoretical curve. While this deviation is slight (19% and 20% respectively), it was hypothesized that this was the start of a new data trend where mutual irradiation at the base of the convex dimple was starting to mitigate the effects of increased sur-

face area, and therefore a theoretical limit to the improvement of the radiative heat transfer could be placed. Specimens with even more convex dimples on the surface were designed but could not be simulated due to the computational limitation at YSU to see if this hypothesis would bear fruit. Therefore, a new study was devised in order to explore this hypothesis in greater detail while circumventing some of the computational limitations placed on this study.
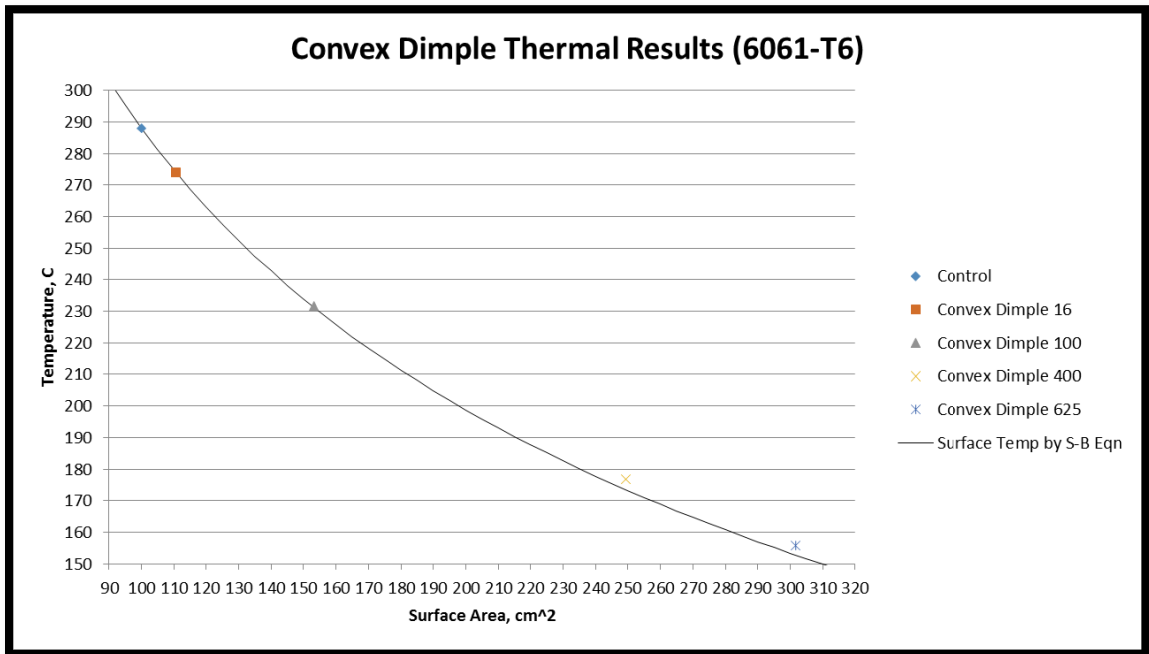
Figure 39: Convex Dimple Thermal Results

50

Convex Dimple Thermal Results (6061-T6)						
Specimen	Surface Area (sq. cm)	Volume (cubic cm)	Base Temp (Celsius)	Average Surface Temp (Celsius)	Normalized Surface Area	Temp Difference
Control	100.00	100.00	288.20	287.92	1.00	0.28
Convex Dimple 16	110.56	72.22	274.23	274.03	1.11	0.20
Convex Dimple 100	153.16	72.22	231.92	231.79	1.53	0.13
Convex Dimple 400	249.44	72.22	176.90	176.76	2.49	0.14
Convex Dimple 625	301.75	72.22	155.99	155.86	3.02	0.13

5.1.3 196 Convex Numerical Simulation Results and Discussion (Study 3)

For this final numerical simulation study, changes, and/or improvements, were made to incorporate knowledge gained from the previous two studies. In study 2, the overall bounding box of 10cm x10cm x 1cm was held constant leading to a decrease in volume as the surface area increased. In attempt to, in a sense, to equalize the effects of conduction the volume was held constant at 100 cm^3 and a slight relaxation of the bounding box was made. This is a rudimentary attempt to equalize the conductive lengths across all specimens, and it is reasoned that since conduction is at its heart a volumetric phenomenon, that equalizing the volume would in a macro sense equalize conductive paths. As mentioned in chapter 4, the surface was fixed to 196 protrusions where the surface area was modified using the parameters given by a two-term cosine expansion. Again the material was changed back to an ABS polymer for this study.

Figures 40, 41, and 42 illustrate the variation of temperature through the specimens sectioned at centerline. The temperature in the figures appears to vary linearly from the base (source) to the surface (sink). While these simulations can be

51

viewed as 1-dimensional heat transfer and would have a linear temperature distribution, the irregular surface geometry and nonlinear boundary conditions should intuitively introduce some nonlinearity in the region near the surface. There is some reasoning as to why this is being seen in the figures. First is an artifact to the software itself, in order to show a smooth transition of temperatures over a wide range some of the differential detail in the region of interest is lost in that action. Secondly, the extremely low thermal conductivity of ABS acts to diffuse the temperatures, especially in a steady-state analysis. In an attempt to mitigate the effects of thermal conductivity, Figure 43 looks at the temperature gradient inside the specimen. Circled in Figure 43 are areas where the temperature gradient was slow at the surface and just below the surface increased dramatically in order to preferentially move heat to a more effective portion of the surface. It is in these highlighted spots where the effects of mutual irradiance can be seen.
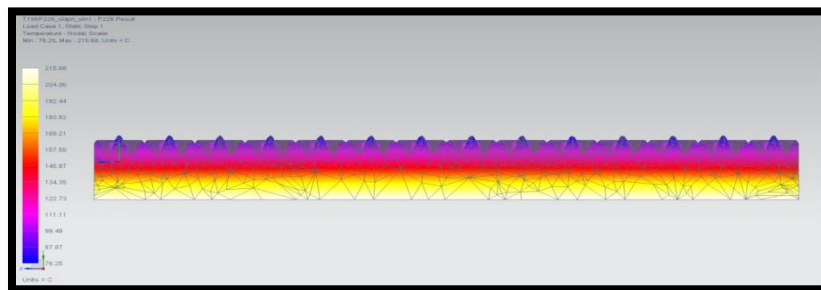
Figure 40: T196P226 Temperature Results (Sectioned at Centerline)
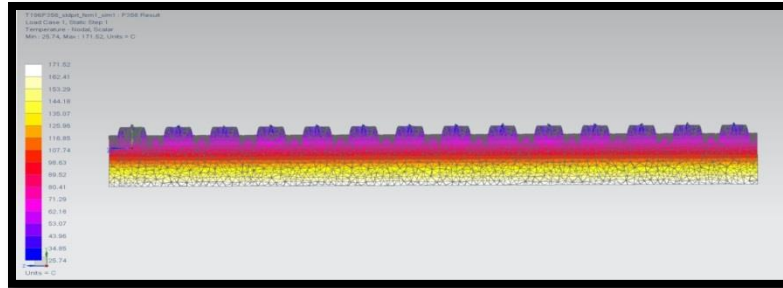
Figure 41: T196P356 Temperature Results (Sectioned at Centerline)
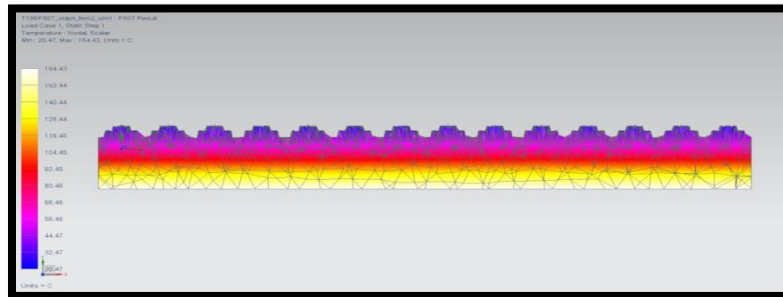
Figure 42: T196P507 Temperature Results (Sectioned at Centerline)
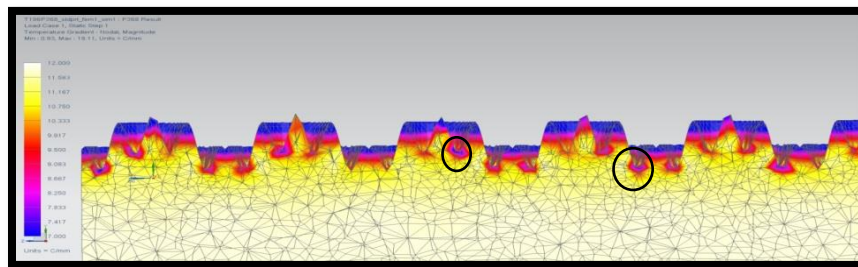
Figure 43: T196P368 Temperature Gradient (Magnitude, Sectioned at Centerline)

Figure 44 graphically depicts the results the numerical simulations, and includes the max/min/average at both the surface and at the base of the specimen. The theoretical temperature given by the Stefan-Boltzmann equation is also included. The tabular data is provided in Table 9.
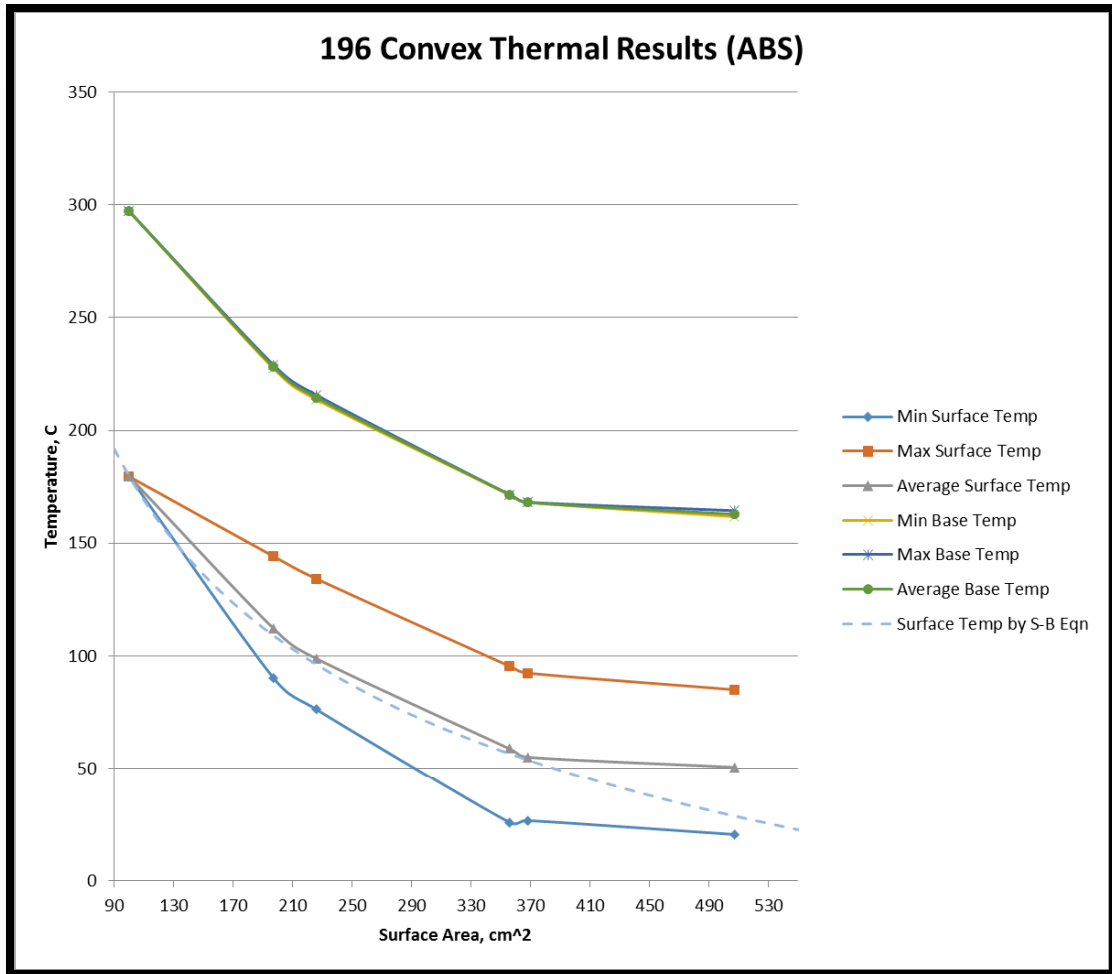
Figure 44: 196 Convex Thermal Results

The average temperature of the surface trends very closely with the data received

from the simulations except for the last data point, T196P507. This data point devi-

ates from the Stefan-Boltzmann curve by approximately 74.5%, which is significant

in the eyes of this author. However, there are some mitigating factors to this result.

As stated previously, the mesh for T196P507 was poor in the sense that it did not

completely conform to the CAD generated geometry. This also means that a mesh

convergence study was not, and could not be, performed for any of these data. The

last mitigating factor is that the deviation is only represented by one data point, and

for a clear cut trend need more points of deviation are required. However, this data point at least, when compared to the previous studies, represents significant departure from what is theoretically prescribed.

196 Convex Thermal Results (ABS)								
			Base Temp (Celsius)			Surface Temp (Celsius)		
Specimen	Surface Area (cm^2)	Volume (cm^3)	Min	Max	Average	Min	Max	Average
Control	100.00	100.00	297.20	297.20	297.20	179.55	179.55	179.55
T196P197	197.00	100.00	227.61	229.12	228.29	90.31	144.22	112.26
T196P226	226.00	100.00	213.77	215.68	214.66	76.26	134.22	98.80
T196P356	356.00	100.00	171.43	171.52	171.50	25.74	95.44	58.77
T196P368	368.00	100.00	168.15	168.25	168.11	26.62	92.43	55.07
T196P507	507.00	100.00	161.77	164.43	162.86	20.47	85.05	50.57

5.2 Experimental Results and Discussion

For the experimental portion, four vertically printed (Z orientation) samples were run in the vacuum chamber: The control specimen, T196P356, T196P436, and T196P507. The specimens were run consistently to the experimental procedure outlined in chapter 4. The results of these tests are depicted in Figures 45-48. In those figures HP is the hot plate thermistor temperature, PS is the panel surface thermistor temperature, and Vout TP is the thermopile output voltage.
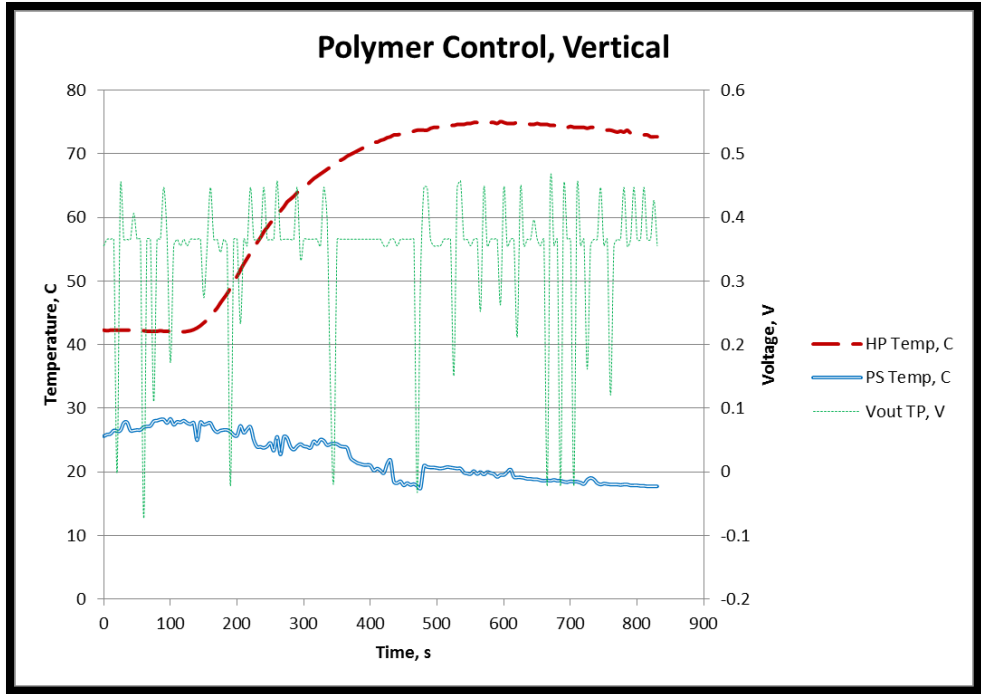
Figure 45: Experimental Control Results
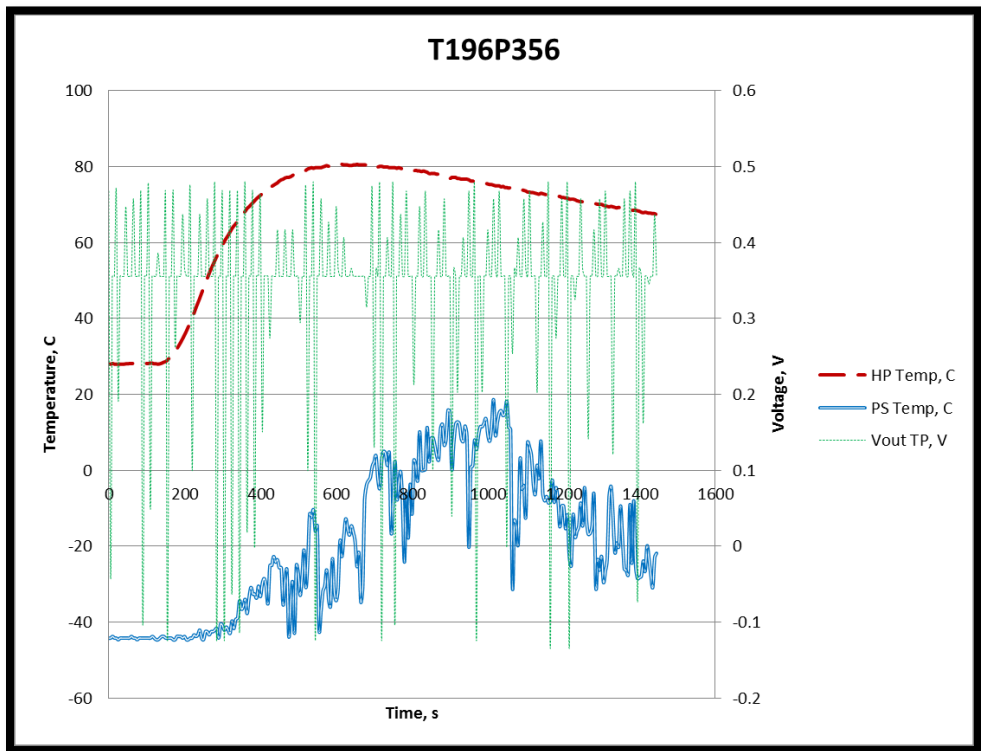
Figure 46: T196P356 Experimental Results
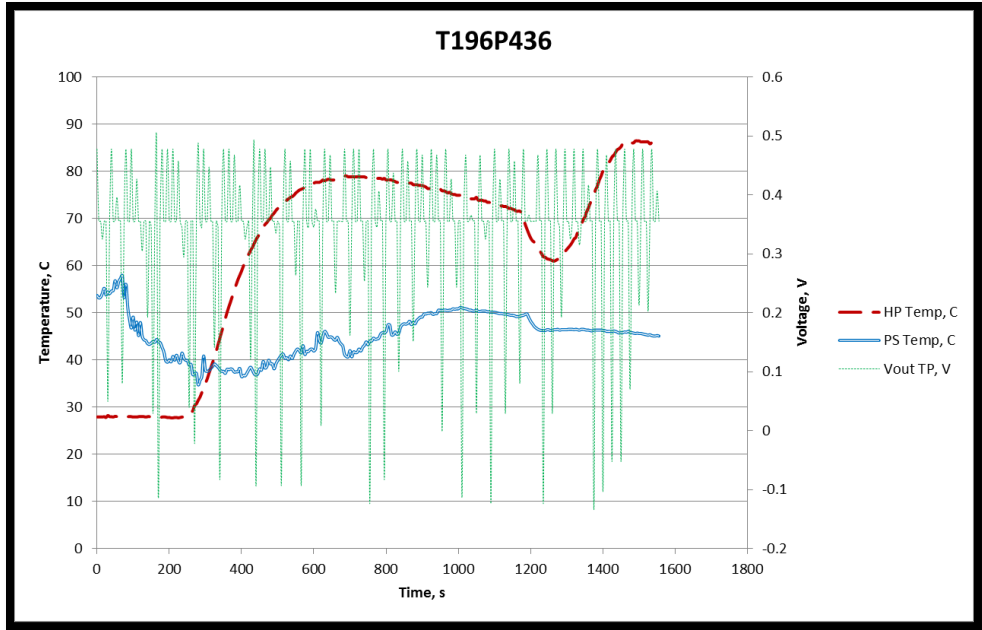
Figure 47: T196P436 Experimental Results
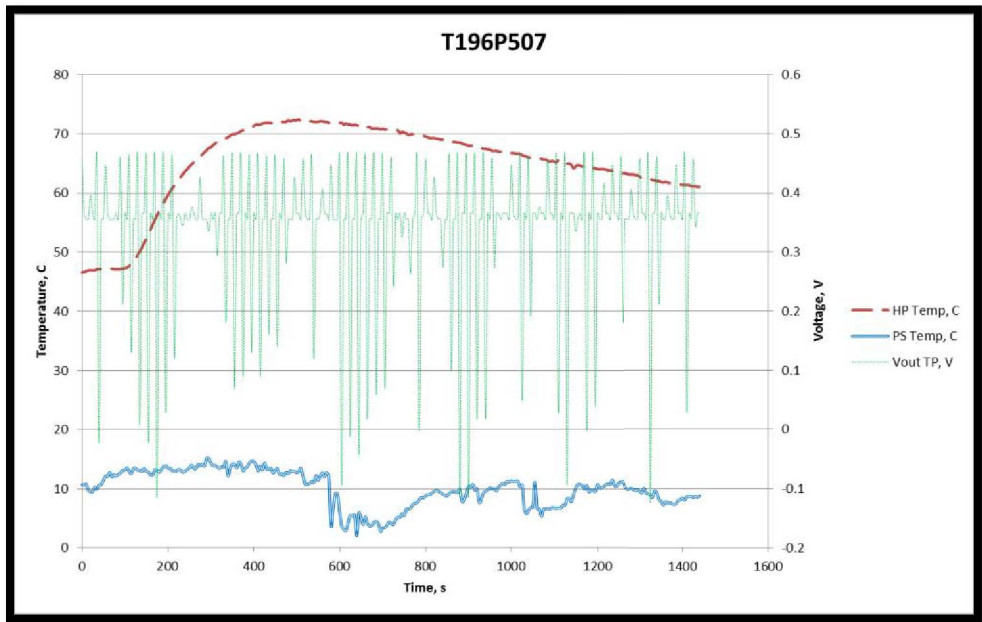
Figure 48: T196P507 Experimental Results

57

The experiment left much to be desired. As it was a completely new design implementation, there were many issues still needing to be resolved. The hot plate thermistor data is free of electrical noise and very consistent between tests and should be regarded as quality data. The only problem with the hot plate thermistor data is the lack of a steady state operating condition which is mostly likely due to the hot plate's rudimentary temperature control. The panel thermistor also has a few issues. Electrical noise being the first and is thought to be attributed to small wire movements due to leakage in the chamber and essentially an oscillating airflow condition. Secondly, it came to light that the printed specimen were not completely flat, and so the location of the thermistor on the specimen may not have over top of a portion directly contacting the hot plate leading to more error and dependence on transient effects. Lastly, a good point was raised after the experiments that no conductive grease was used at the specimen-hot plate interface and is definitively leading to error at the panel thermistor. The thermopile data suffered from a very electrically noisy signal. The thermopile itself came with a testing certification from the manufacturer and was wired correctly by YSU's Electronic Maintenance Services (EMS). The thermopile was operating, but the device works on very small voltage changes (µV scale) that even with an amplifier may too sensitive for the NI-DAQ. Also, the thermopile voltage was supplied by the NI-DAQ and may not be as constant of a voltage supply as originally thought adding to the signal noise. A test on the NI-DAQ signal voltage is required to quantify the possible error.

In order to glean something useful from the experiments, the thermopile data was clipped from the point of maximum temperature as read by the hot plate ther-

mistor to the end of the test. This was done to contain only data at the time of the

test where radiation heat transfer should be a maximum. The shortened data was

then processed by a discrete fast Fourier transform and subsequently converted and

plotted as a power spectral density. The aim was analysis the amount of energy con-

tained in the signal for comparison between the experiments. This is summarized in

the simple table below.

Table 10: PSD of Thermopile Data

Power Spectral Density of Thermopile Data	
Specimen	Magnitude
Control	6.5248
T196P356	30.1857
T196P436	10.2424
T196P507	15.9022

The magnitude of the power spectral density does trend upward in response to in-

creased surface area, but then dips in intensity where in Figure 44 the deviation

from the Stefan-Boltzmann equation starts to occur. It should be noted that this may

be a bias, forceful use of mathematics to correlate the numerical simulation data in

some way to the experimental data.

Chapter 6: Conclusions and Future Work

With regards to the experiment, while the data taken could not be used to validate the numerical simulations the experiment did provide useful knowledge. That knowledge was in the future changes to the experimental setup that will allow for validation of the numerical simulations. Some of these corrections were mentioned previously in chapter 5, but additional measures need to be taken. First, adding extra thermistors and/or thermocouples to measure ambient air temperature in the chamber as well as the surface temperature of the liquid nitrogen heat sink. Second, sealing of the heat sink itself was an issue and needs to be addressed. The heat sink was originally designed with a tapered, machined ledge with a corresponding groove machined in the mating part to provide a tight taper seal. For easy of machining this taper ledge and groove was changed to have straight walls, meaning that only the tension of the fasteners on the heat sink would be creating the seal. Even though a tight tolerance was held on the ledge and groove, the fasteners, which were only threaded into the HDPE lid, could not provide enough tension for proper sealing. Simply adding a cold tolerant sealant to the ledge and groove and using stainless-steel helicoils in the HPPE lid to allow for proper fastener tension should fix the problem. Lastly, signal filtering on the data streams is most likely necessary. With those fixes in place, the entire experiment then needs a validation test case. Future work could also include fitting the test chamber with an infrared camera to measure surface temperature variation of the specimen instead of the thermopile. This could be accomplished by fitting a new lid with a sight window for the infrared camera to view the specimen through while keeping the camera itself out of the

vacuum chamber. The infrared camera data could then be turned into surface data to directly compare to the output of the numerical simulations. The addition of the infrared camera would provide more point specific information about how the panels are performing and would enhance the experiment.

The results of the numerical simulations, in particular the 196 Convex specimens, show that specimen T196P507 performed the best and had the lowest base and surface temperatures with a 45% and 72% reduction in base and surface temperature, respectively, over the control panel (flat planar geometry). That said, in Figure 44, in can be seen that none of the specimens have a base temperature below that of the glass transition temperature, 108 ^{0}C, of ABS. The glass transition temperature is the point where the polymer material reverts back to a molten or rubber-like state and its mechanical properties can be severely degraded. This is obviously not an ideal outcome. Also, the glass transition temperature is still above that of the max recommended operating temperature for general electronics, 85 ^{0}C.

However, there is a remedy to this situation. It should be noted that specimens from 196 Convex set were held to a fixed volume and relaxing this constraint to shorten the conductive pathways, i.e. thinning the specimen base, will reduce base temperature. As an example using the theoretical heat transfer equations, if the thickness remains unaltered the required surface area would roughly need to be 1258 cm^2 for a base temperature of 85 ^{0}C. That surface area is close to 2.5 times the amount of the best performing specimen and seems unfeasible for practical purposes. If the thickness is reduced by half, the required surface area is 524 cm^2 which is

very close to that of specimens tested. It seems very feasible that just with small edits the two-term cosine expansion and a reduction of thickness, that 20W of waste heat can be rejected by the radiator while maintaining the electronics at a manageable temperature.

It is these edits to the specimens that in the future would be the basis for another set of numerical simulations. Also in the future, exploration into a produce a unit cell version of the surface topology as means not only to non-dimensionalize the problem but also to reduce computation effort should be investigated.

Also of note is the 79% departure of specimen T196P507 from the surface temperature given by the theoretical Stefan-Boltzmann curve. This may suggest that there exists a practical limit to radiation heat transfer with respect to the increase of surface area. Surface temperature as a function of surface area of the Stefan-Boltzmann curve dictates that in the limit as this surface area becomes very large that it is theoretically possible to reach absolute zero temperature. Mutual irradiance of a surface to itself may be nature's way of guarding against this possibility of heat transfer in such an efficient manner that a zero energy state is reached. It would be of interest to explore this hypothesis in detail for the future.

References

1. **Wertz, James R., Everett, David F. and Puschell, Jeffrey j.** *Space Mission Engineering: The New SMAD.* s.l. : Microcosm, 2011.

2. *Linearized Techniques for Solving the Inverse Problem In the Satellite Thermal Control.* **Arduini, C., Laneve, G. and Folco, S.** 9-10, 1998, Acta Astronautica, Vol. 43, pp. 473-479.

3. *Nonlinear analysis of a simple model of temperature evolution in a satellite.* **Gaite, Jose, Sanz-Andres, Angel and Perez-Grande, Isabel.** 2009, Nonlinear Dynamics, Vol. 58, pp. 405-415.

4. *Nonlinear Analysis of Space Craft Thermal Models.* **Gaite, Jose.** s.l. : Springer Science + Business Media, 2011, Nonlinear Dynamics, Vol. 65, pp. 283-300.

5. *Analytical Study of the Thermal Behaviour And Stability Of a Small Satellite.* **Perez-Grande, Isabel, et al., et al.** s.l. : Elsevier Ltd., 2009, Applied Thermal Engineering, Vol. 29, pp. 2567-2573.

6. **Karam, Robert D.** *Satellite Thermal Control for Systems Engineers.* Reston : American Institute of Aeronautics and Astronautics, Inc., 1998. Vol. 181.

7. *Mathematical Model Validation Of a Thermal Architecture System Connecting East/West Radiators by Flight Data.* **Torres, Alejandro, Mishkinis, Donatas and Kaya, Tarik.** s.l. : Elsevier Ltd., 2014, Applied Thermal Engineering, Vol. 66, pp. 1-14.

8. *Heat Capacity Estimation Of the Thermal Buffer Mass For Temperature Control Of Satellite Electronic Components In Periodic Operation.* **Kim, T. Y.** s.l. : Elsevier Masson SAS, 2013, Aerospace Science and Technology, Vol. 30, pp. 286-292.

9. *Optimization of a Space Radiator with Energy Storage.* **Roy, Sanjay K. and Avanic, Branko L.** s.l. : Elsevier Ltd., 2006, International Communications in Heat and Mass Transfer, Vol. 33, pp. 544-551.

10. **Cengel, Yunus A.** *Heat and Mass Transfer: A Practical Approach.* New York : McGraw-Hill Companies, Inc., 2007.

11. *Optimum Isothermal Surfaces That Maximize Heat Transfer.* **Leontiou, Theodoros, Kotsonis, Marios and Fyrillas, Marios M.** s.l. : Elsevier Ltd., 2013, International Journal Of Heat and Mass Transfer, Vol. 63, pp. 13-19.

12. **Seigel, Robert and Howell, John R.** *Thermal Radiation Heat Transfer.* Washington, D.C. : Taylor & Francis, Inc., 1992.

13. **Patankar, Suhas V.** *Numerical Heat Transfer and Fluid Flow.* Washington : Hemisphere Publishing Corporation, 1980.

14. **Zienkiewicz, O. C. and Morgan, Kenneth.** *Finite Elements and Approximation.* New York : John Wiley & Sons, Inc., 1983.

15. *Transient Non-Linear Heat Conduction-- Radiation Problems-- A Boundary Element Formulation.* **Blobner, Jutta, Bialecki, Ryszard A. and Kuhn, Gunther.** s.l. : John Wiley & Sons, Ltd., 1999, International Journal For Numerical Methods In Engineering, Vol. 46, pp. 1865-1882.

16. **Bialecki, R.A.** *Solving Heat Radiation Problems Using the Boundary Element Method.* Southampton : Computational Mechanics Publications, 1993.

17. *Topological Sensitivity Analysis for Two-Dimensional Heat Transfer Problems Using the Boundary Element Method.* **Anflor, C. T.M. and Marczak, R. J.** s.l. : Springer International, 2013, Advanced Structural Materials, Vol. 43, pp. 11-33.

18. *Cubic Bezier Splines for BEM Heat Transfer Analysis of the 2-D Continuous Casting Problems.* **Cholewa, R., et al., et al.** s.l. : Springer-Verlag, 2002, Computational Mechanics, Vol. 28, pp. 282-290.

19. **ASTM International.** Standard Terminology for Additive Manufacturing Technologies. [Online] March 2012. http://www.astm.org/FULL_TEXT/F2792/HTML/F2792.htm. F2792-12a.

20. **Gibson, Ian, Rosen, David and Stucker, Brent.** *Additive Manufacturing Technologies.* 2nd. New York : Springer Science+ Business Media, 2015.

21. *Improved Mechanical Properties of Fused Deposition Modeling-Manufactured Parts Through Build Parameter Modifications.* **Hossain, Mohammad Shojib, et al., et al.** 6, s.l. : Journal of Manufacturing Science and Engineering, 2014, Vol. 136.

22. Emissivity Values for Common Materials. [Online] http://www.infrared-thermography.com/material-1.htm.

23. **3D Systems, Inc.** *StereoLithography Interface Specification.* October 1989.